

The MAGPI Survey: the evolution and drivers of gas turbulence in intermediate-redshift galaxies

Yifan Mai^{1,2}★, Scott M. Croom^{1,2}, Emily Wisnioski^{2,3}, Sam P. Vaughan^{2,4,5,6}, Mathew R. Varidel⁷, Andrew J. Battisti^{2,3}, J. Trevor Mendel^{2,3}, Marcie Mun^{2,3}, Takafumi Tsukui^{2,3}, Caroline Foster^{2,8}, Katherine E. Harborne^{2,9}, Claudia D. P. Lagos^{2,9}, Di Wang^{1,2}, Sabine Bellstedt⁹, Joss Bland-Hawthorn^{1,2}, Matthew Colless^{2,3,10}, Francesco D'Eugenio^{11,12}, Kathryn Grasha[†], Yingjie Peng^{13,14}, Giulia Santucci^{2,9}, Sarah M. Sweet^{2,15}, Sabine Thater¹⁶, Lucas M. Valenzuela¹⁷ and Bodo Ziegler¹⁶

¹*Sydney Institute for Astronomy (SfA), School of Physics, The University of Sydney, NSW 2006, Australia*

²*ARC Centre of Excellence for All Sky Astrophysics in 3 Dimensions (ASTRO 3D)*

³*Research School of Astronomy and Astrophysics, Australian National University, Canberra, ACT 2611, Australia*

⁴*Astronomy, Astrophysics and Astrophotonics Research Centre, Macquarie University, Sydney, NSW 2109, Australia*

⁵*School of Mathematical and Physical Sciences, Macquarie University, NSW 2109, Australia*

⁶*Centre for Astrophysics and Supercomputing, School of Science, Swinburne University of Technology, Hawthorn, VIC 3122, Australia*

⁷*Brain and Mind Centre, The University of Sydney, NSW 2006, Australia*

⁸*School of Physics, University of New South Wales, Sydney, NSW 2052, Australia*

⁹*International Centre for Radio Astronomy (ICRAR), M468, The University of Western Australia, 35 Stirling Highway, Crawley, WA 6009, Australia*

¹⁰*Sub-Department of Astrophysics, Department of Physics, University of Oxford, Denys Wilkinson Building, Keble Road, Oxford OX1 3RH, UK*

¹¹*Kavli Institute for Cosmology, University of Cambridge, Madingley Road, Cambridge CB3 0HA, UK*

¹²*Cavendish Laboratory, University of Cambridge, 19 JJ Thomson Avenue, Cambridge CB3 0HE, UK*

¹³*Department of Astronomy, School of Physics, Peking University, 5 Yiheyuan Road, Beijing 100871, People's Republic of China*

¹⁴*Kavli Institute for Astronomy and Astrophysics, Peking University, 5 Yiheyuan Road, Beijing 100871, People's Republic of China*

¹⁵*School of Mathematics and Physics, University of Queensland, St Lucia, Queensland 4072, Australia*

¹⁶*University of Vienna, Department of Astrophysics, Türkenschanzstraße 17, 1180 Vienna*

¹⁷*Universitäts-Sternwarte, Fakultät für Physik, Ludwig-Maximilians-Universität München, Scheinerstr. 1, 81679 München, Germany*

Accepted 2024 August 20. Received 2024 August 8; in original form 2024 May 16

ABSTRACT

We measure the ionised gas velocity dispersions of star-forming galaxies in the MAGPI survey ($z \sim 0.3$) and compare them with galaxies in the SAMI ($z \sim 0.05$) and KROSS ($z \sim 1$) surveys to investigate how the ionised gas velocity dispersion evolves. For the first time, we use a consistent method that forward models galaxy kinematics from $z = 0$ to $z = 1$. This method accounts for spatial substructure in emission line flux and beam smearing. We investigate the correlation between gas velocity dispersion and galaxy properties to understand the mechanisms that drive gas turbulence. We find that in both MAGPI and SAMI galaxies, the gas velocity dispersion more strongly correlates with the star-formation rate surface density (Σ_{SFR}) than with a variety of other physical properties, and the average gas velocity dispersion is similar, at the same Σ_{SFR} , for SAMI, MAGPI and KROSS galaxies. The results indicate that mechanisms related to Σ_{SFR} could be the dominant driver of gas turbulence from $z \sim 1$ to $z \sim 0$, for example, stellar feedback and/or gravitational instability. The gas velocity dispersion of MAGPI galaxies is also correlated with the non-rotational motion of the gas, illustrating that in addition to star-formation feedback, gas transportation and accretion may also contribute to the gas velocity dispersion for galaxies at $z \sim 0.3$. KROSS galaxies only have a moderate correlation between gas velocity dispersion and Σ_{SFR} and a higher scatter of gas velocity dispersion with respect to Σ_{SFR} , in agreement with the suggestion that other mechanisms, such as gas transportation and accretion, are relatively more important at higher redshift galaxies.

Key words: galaxies: evolution – galaxies: kinematics and dynamics – galaxies: ISM.

1 INTRODUCTION

The evolution of the bulk gas motions within galaxies with cosmic time is governed by the complex interplay of different internal and

★ E-mail: yifan.mai@sydney.edu.au

† ARC DECRA Fellow

external physical processes such as gravity, feedback, cooling, gas accretion and galaxy interactions (e.g. Bower et al. 2006; Dekel et al. 2009; Bouché et al. 2010; Davé et al. 2012; Genel et al. 2012; Lilly et al. 2013; Gabor & Bournaud 2014; Schaye et al. 2015; Sillero et al. 2017; Bird et al. 2021; Forbes et al. 2023). Galaxy kinematic properties are important tools to help us understand the evolution of galaxies from the early Universe to the present time and to constrain galaxy evolution models (e.g. review by Cappellari 2016).

The velocity dispersion of ionised gas within disk galaxies decreases with cosmic time (Kassin et al. 2012; Wisnioski et al. 2015; Johnson et al. 2018; Übler et al. 2019), from $\sim 50 \text{ km s}^{-1}$ in galaxies at $z > 1$ to $\sim 20 \text{ km s}^{-1}$ in the local universe (Genzel et al. 2006; Epinat et al. 2008; Law et al. 2009; Green et al. 2014; Moiseev et al. 2015a; Varidel et al. 2020; Law et al. 2022). The thermal broadening of star-forming gas traced by the $\text{H}\alpha$ emission line due to a characteristic temperature of 10^4 K is estimated to be 11.7 km s^{-1} (Bland-Hawthorn et al. 2024)¹. However, the ionised gas velocity dispersion observed at all epochs is greater than this value. The gas velocity dispersion above the thermal contribution must arise from other local or global processes which induce turbulence in the gas. Two questions thus arise: What are the main drivers of turbulence in ionised gas and how do the physical processes that induce turbulence evolve with cosmic time?

The main drivers of high gas velocity dispersion over cosmic time are not well constrained. Disk galaxies in a state of equilibrium must maintain a balance between the energy loss by turbulent dissipation and energy injection from other local and global mechanisms (Krumholz et al. 2018). Global or external mechanisms that may induce higher turbulence include gas accretion (Klessen & Hennebelle 2010; Aumer et al. 2010) and minor mergers (Bournaud et al. 2009). Possible internal mechanisms of gas turbulence include star-formation feedback (e.g. Green et al. 2010; Faucher-Giguère et al. 2013; Green et al. 2014; Moiseev et al. 2015b; Bacchini et al. 2020; Egorov et al. 2023), gravitational instability (e.g. Krumholz & Burkhardt 2016; Krumholz et al. 2018; Molina et al. 2020) and interactions between different galaxy components (Aumer et al. 2010; Oliva-Altamirano et al. 2018).

Star-formation feedback is widely considered to be a significant source of gas turbulence, both theoretically (Ostriker et al. 2010; Ostriker & Shetty 2011; Faucher-Giguère et al. 2013; Krumholz & Burkhardt 2016; Krumholz et al. 2018; Bacchini et al. 2020) and in simulations (e.g. Shetty & Ostriker 2012; Rathjen et al. 2023; Hung et al. 2019). Stellar feedback injects energy and momentum into the interstellar medium through supernovae, stellar winds, radiation pressure and ionising radiation. A correlation between star formation rate (SFR) and gas velocity dispersion has been found in many observational studies (e.g. Green et al. 2010, 2014; Zhou et al. 2017; Varidel et al. 2020; Law et al. 2022), providing evidence for the role of stellar feedback in increasing the local turbulence in disks and therefore the measured disk velocity dispersion.

However, the degree of importance of stellar feedback in driving gas turbulence is debated. Some studies proposed that star formation alone can explain the gas velocity dispersion we observe (Bacchini et al. 2020; Faucher-Giguère et al. 2013; Egorov et al. 2023), while other studies suggested that stellar feedback can only drive part of the gas velocity dispersion, thus other mechanisms are needed (Zhou et al. 2017; Bik et al. 2022; Forbes et al. 2023; Kim et al. 2013; Dib et al. 2006; Shetty & Ostriker 2012). Gravitational instability

(Krumholz & Burkhardt 2016; Krumholz et al. 2018), gas accretion (Klessen & Hennebelle 2010) and galaxy interaction (Bournaud et al. 2009) have been suggested as possible sources of the additional gas turbulence.

The importance of different mechanisms may vary with redshift and environment. Gas accretion at high redshift was more efficient in converting bulk kinetic energy into turbulent kinetic energy than at low redshifts (Klessen & Hennebelle 2010; Ginzburg et al. 2022). A simulation study by Jiménez et al. (2023) showed that stellar feedback is more important for galaxies in lower halo masses and at lower redshift. Krumholz et al. (2018) predicts that the relation between gas velocity dispersion and SFR changes with the fraction of the interstellar medium that is in the star-forming molecular phase, which in turn depends on redshift.

The measurement of intrinsic gas velocity dispersion is challenging. Ionised gas velocity dispersion is normally measured based on the width of emission lines, such as the $\text{H}\alpha$ emission line. However, the measurement of line width within a dynamic system like a disk is complicated by observational and instrumental factors including the line spread function (LSF), spaxel grid, and the size and shape of the point spread function (PSF) (Davies et al. 2011; Oh et al. 2022). The beam smearing caused by the Earth's atmosphere blurs light between neighbouring spaxels. If there is a velocity difference between neighbouring spaxels, the beam smearing artificially broadens emission lines, thus increasing the apparent gas velocity dispersion. The beam smearing is the strongest at the centre of galaxies, where the velocity gradient is the largest.

Several different methods have been applied to minimise or account for the beam smearing. Johnson et al. (2018) applied a correction to gas velocity dispersion based on galaxy size, seeing PSF and velocity gradient. ^{3D}BAROLO (Di Teodoro & Fraternali 2015), GalPaK^{3D} (Bouché et al. 2015) and GBKFIT (Bekiaris et al. 2016) use model-fitting techniques to model the flux and kinematics of galaxy three-dimensional data cubes, including beam smearing effects. ^{3D}BAROLO uses a tilted-ring model that assumes a galaxy is a thin disc and consisting of concentric rings with different rotational velocity and flux. GalPaK^{3D} and GBKFIT assume parametric radial flux distributions and velocity profiles.

In this study, we use the code BLOBBY3D (Varidel et al. 2019) which employs a forward modelling technique that models the gas kinematics and substructures simultaneously. The advantage of BLOBBY3D is that it does not assume any given gas structure, but decomposes the gas distribution into a number of Gaussian ‘blobs’. The number of blobs is flexible and depends on the complexity of the observed gas substructure. BLOBBY3D has been shown to recover the intrinsic gas velocity dispersion better than other modelling techniques where there is sufficient signal-to-noise (S/N). More constrained techniques, such as ^{3D}BAROLO and GalPaK^{3D}, may work better where S/N is poor.

Different surveys have employed various measurement techniques to measure the intrinsic gas velocity dispersion in galaxies across cosmic epochs. For example, Übler et al. (2019) measured the gas velocity dispersion of galaxies at $z > 0.6$ by forward-modelling the one-dimensional velocity and velocity dispersion profile. Law et al. (2022) corrected for the effects of beam smearing using estimates derived from a three-dimensional model that is constructed based on the observed velocity field of each galaxy for low redshift galaxies ($z \sim 0.05$). The systematic difference between the surveys makes it difficult to constrain the evolution of gas velocity dispersion.

The most rapid change in gas velocity dispersion seems to occur from $z \sim 1$ to $z \sim 0$ (Wisnioski et al. 2015; Übler et al. 2019; Kassin et al. 2012). Previous studies measured the ionised gas velocity dis-

¹ This value assumes a mean molecular weight made up of 74% H, 24% He and 2% for all other metals, typical of the modern day ISM.

persion for many local galaxies from the Integral Field Spectroscopy (IFS) survey such as SAMI (Varidel et al. 2020) and MaNGA (Yu et al. 2019; Law et al. 2022) and high redshift galaxies at $z > 0.6$ such as KMOS^{3D} (Übler et al. 2019). Kassim et al. (2012) used the slit-based DEEP2 survey to investigate the evolution of gas velocity dispersion of galaxies at $0.2 < z < 1.2$. However, the gas velocity dispersion from IFS data between $0 < z < 1$, at which most of the change of gas velocity dispersion happens, has not been investigated in a self-consistent manner.

In this study, we will measure the ionised gas velocity dispersion of galaxies from the Middle Ages Galaxy Properties with Integral Field Spectroscopy (MAGPI) survey (Foster et al. 2021) at $z \sim 0.3$, to fill the gap of the IFS measurement of gas velocity dispersion at intermediate redshift, and to link SAMI galaxies (Bryant et al. 2015) at $z \sim 0.05$ and KROSS galaxies (Stott et al. 2016) at $z \sim 1$. We measure the gas velocity dispersion from these three surveys in a consistent manner, enabling a detailed exploration of how gas kinematics evolved over the past 8 billion years. In Section 2, we describe the MAGPI survey, data reduction and our sample selection. In Section 3, we describe the methods used to measure the gas velocity dispersion. In Section 4, we present our results for MAGPI gas velocity dispersions, investigate their relations with galaxy properties and compare them with other surveys. In Section 5, we discuss the evolution of gas velocity dispersion and drivers of gas turbulence. In Section 6, we summarise our results.

Throughout this paper, we adopt the concordance cosmology ($\Omega_\Lambda = 0.7$, $\Omega_m = 0.3$, $H_0 = 70 \text{ km s}^{-1} \text{ Mpc}^{-1}$).

2 DATA

2.1 The MAGPI Survey

Data used in this work are drawn from the MAGPI survey (Foster et al. 2021). MAGPI makes use of the ground layer adaptive optics (GLAO) aided, wide-field optical integral field spectrograph, the Multi Unit Spectroscopic Explorer (MUSE; Bacon et al. 2010), mounted at the European Southern Observatory Very Large Telescope (VLT). MUSE has a $1 \times 1 \text{ arcmin}^2$ field-of-view (FOV) sampled at $0.2 \times 0.2 \text{ arcsec}^2$. The typical full width at half maximum (FWHM) of MUSE PSF is $\sim 0.6 \text{ arcsec}$. The spectroscopic observations from the MAGPI survey cover the wavelength ranges $4700\text{--}9351 \text{ \AA}$ with a spectral resolution of $R = 2728$ at 7025 \AA .

The MAGPI survey targets 60 massive central galaxies (primary galaxies) and their neighbouring galaxies (secondary galaxies) within the MUSE FOV. The targets are selected from G12, G15 and G23 fields in the Galaxy And Mass Assembly (GAMA) survey (Driver et al. 2011). At the time of writing, the MAGPI survey has completed the observation of 48 fields, among which 35 fields have been fully reduced with relevant data products. There are 780 passive and star-forming galaxies in the redshift range of interest ($0.22 < z < 0.42$), of which 180 have $H\alpha$ -based SFR measurement.

2.1.1 Galaxy properties

We use the Galaxy Integral Field Unit (IFU) Spectroscopy Tool (GIST; Bittner et al. 2019) to fit emission lines and continuum spectra in MAGPI galaxies (Battisti et al. in prep). GIST is a Python wrapper designed to run the Penalized PiXel-Fitting (pPXF; Cappellari & Emsellem 2004; Cappellari 2017) method on IFS data. GIST can extract stellar kinematics, conduct emission-line analysis, and deduce stellar population properties through spectral fitting. We use the $H\alpha$

flux map in GIST to calculate the half-light radius (R_e) of MAGPI galaxies as the tracer of star-forming R_e , inside which half the stars are currently forming. However, we note that $H\alpha R_e$ can be different to star-forming R_e if extinction significantly varies across the galaxy. At low surface brightness $H\beta$ may not have sufficient S/N to get a reliable extinction correction, so we use non-extinction corrected $H\alpha R_e$. We generate the inclination corrected curve of growth of $H\alpha$ flux as a function of radius and define the radius enclosing 50% of the flux as R_e , to clarify that this is effectively the major axis R_e , not circularly averaged. Throughout this paper, R_e represents the half-light radius of $H\alpha$ flux unless specified otherwise.

BLOBBY3D requires stellar continuum-subtracted data. We subtract the stellar continuum from the MUSE spectrum using the stellar continuum fitting products from GIST. The stellar continuum fits were done on a spaxel level. Initial estimates of the stellar continuum were performed with the emission line masked, and those initial estimates were then used to fit the stellar continuum and emission line using templates from flexible stellar population synthesis (FSPS; Conroy et al. 2009, 2010; Conroy & Gunn 2010) and the multiplicative Legendre polynomial is set to 12 (Battisti et al. in prep).

We use the Baldwin, Phillips & Terlevich (BPT; Baldwin et al. 1981; Kewley et al. 2001; Kauffmann et al. 2003) ionization diagnostics to identify star-forming (SF), active galactic nucleus (AGN) and composite spaxels in galaxies and to classify galaxies. We use the line ratios $[\text{NII}]\lambda 6584/H\alpha$ and $[\text{OIII}]\lambda 5007/H\beta$, including only spaxels that have $S/N > 3$ in all emission lines. The flux and error of these four emission lines are estimated using GIST (Bittner et al. 2019, Battisti et al. in prep) from 50 Monte Carlo realisations of the input data. We remove galaxies that are dominated by AGN and/or composite spaxels ($\geq 50\%$) from our sample. However, we keep the galaxies with AGN and/or composite centre (> 10 spaxels) and star-forming disc (≥ 50 SF spaxels), and identified them as AGN-host galaxies. We mask the AGN and/or composite centres and keep the SF discs for these galaxies. Galaxies that are dominated by SF spaxels are classified as SF galaxies. Some SF galaxies may have a few spaxels at the edge of galaxies classified as composite spaxels due to the low S/N of the $[\text{NII}]\lambda 6584$, $[\text{OIII}]\lambda 5007$ or $H\beta$ emission lines.

SFRs are estimated using the dust-corrected $H\alpha$ luminosity (Kennicutt 1998). $H\alpha$ flux is corrected for extinction using the Balmer decrement on a spaxel by spaxel basis. The extinction curve from Fitzpatrick et al. (2019) is adopted with $R_V = 3.1$. The SFRs are first calculated on a spaxel-by-spaxel basis. The integrated SFRs are then calculated from a sum of the SFRs of all SF spaxels to avoid contamination from AGN (see Mun et al. 2024 for more details). The fraction of SFR missed due to ignoring the AGN/composite spaxels is small. The upper limit on the flux missed (assuming all $H\alpha$ flux is from star formation) is on average only 25% (0.12 dex) for AGN-host galaxies. The SFR surface density (Σ_{SFR}) is calculated as $\Sigma_{\text{SFR}} = \text{SFR}/(2\pi R_e^2)$, in which R_e from $H\alpha$ is used.

The stellar masses are calculated using ProSPECT (Robotham et al. 2020), a package used to analyse star formation history and spectral energy distributions (SED). Photometry over the *ugriZYJHK* bands from GAMA imaging is used to perform ProSPECT SED fitting, assuming a Chabrier (2003) stellar initial mass function (IMF). The stellar population templates by Bruzual & Charlot (2003) are adopted and the dust attenuation law by Charlot & Fall (2000) is applied to correct stellar light attenuation by dust, as outlined in Bellstedt et al. (2020). The stellar mass surface density (Σ_{M_*}) is calculated as $\Sigma_{M_*} = M_*/(2\pi R_e^2)$.

2.1.2 PSF and LSF

The spatial PSF for the MAGPI survey is reconstructed from information generated by the adaptive optics system (Fusco et al. 2020). The advantage of the reconstructed PSF is that it can be obtained for any given time and field, instead of strongly depending on the availability of bright stars. It agrees well with an in-field PSF estimate when a bright star is present (Mendel et al., in prep).

The PSF convolution kernel in BLOBBY3D is a sum of multiple 2D concentric circular Gaussian profiles. We fit the reconstructed PSF with the two-component Gaussian model, which is enough to adequately model the PSF profile. We also test a PSF model using three Gaussian profiles, however this results in just a 1% change in the measured velocity dispersions (i.e., it does not significantly affect our results), but requires 30% more CPU time in running BLOBBY3D.

The spectral LSF is measured from fitting Gaussian profiles to isolated bright skylines, both for a collapsed spectrum of the full field and for every spaxel individually (Bacon et al. 2017, Mendel et al. in prep). The spatial variation of the MUSE LSF is small, so we use the LSF derived from an average spectrum of the full field. The variation of instrumental resolution (σ_{LSF}) between different fields is $0.135 \pm 0.006 \text{ km s}^{-1}$. When we build the BLOBBY3D model for different galaxies, we use the σ_{LSF} based on their field and redshift.

2.1.3 Sample selection

In our preliminary selection, we choose galaxies that have more than 50 spaxels with $H\alpha$ $S/N > 3$. Galaxies with fewer spaxels have less robust resolved kinematics due to beam smearing. Given the typical PSF of MAGPI data (FWHM ~ 0.6 arcsec), 50 pixels correspond to ~ 7 independent resolution elements within the galaxy. The galaxies chosen have redshifts between 0.22 and 0.42. We remove galaxies with clearly disturbed gas kinematics and galaxies with inclination greater than 60° . The intrinsic gas velocity dispersion of high-inclination galaxies is hard to constrain due to the beam smearing (Varidel et al. 2019). Furthermore, BLOBBY3D assumes galaxies have a thin disc and so is not able to model very edge-on galaxies, as the thickness of the galaxy disc becomes prominent for edge-on galaxies so the thin disc model does not work well. There are 110 galaxies in our preliminary sample after applying the above cuts.

2.2 The SAMI Galaxy Survey

The Sydney–AAO Multi-object Integral field spectrograph (SAMI; Croom et al. 2012) uses 13 hexabundles (Bland-Hawthorn et al. 2011) over 1° diameter field-of-view, mounted on the Anglo-Australian Telescope. The SAMI galaxy survey (Bryant et al. 2015; Scott et al. 2018) collected spatially resolved spectra for 3068 galaxies at $0.004 < z < 0.115$ with a broad range in galaxy stellar mass ($\log(M_*/M_\odot) = 10^8$ to 10^{12}). The integral field units were hexabundles (Bland-Hawthorn et al. 2011) that contained 61 fibres that cover 15 arcsec diameter regions on the sky. The wavelength range of SAMI is 3750–5750 Å ($R = 1808$) and 6300–7400 Å ($R = 4304$) for the blue and red arms respectively. Stellar masses are estimated from the rest-frame i -band absolute magnitude and $g - i$ colour, following the method of Taylor et al. (2011) and assuming a Chabrier (2003) IMF.

Varidel et al. (2020) used BLOBBY3D to measure the ionized gas velocity dispersion of 383 star-forming SAMI galaxies. They removed AGN and low-ionization nuclear emission-line region (LINER) galaxies from their sample. They removed galaxies with an inclination greater than 60° . They also removed mergers or galaxies with

clearly disturbed gas kinematics. They applied a mask to spaxels with $H\alpha$ $S/N < 3$ and retained galaxies that had at least 300 unmasked spaxels. They rounded the gas velocity dispersion to the nearest whole number.

Given that both Varidel et al. (2020) and this work employ spatially resolved spectroscopic observational data and utilize the same dispersion measurement methods, we adopt the gas velocity dispersions measured by Varidel et al. (2020) as a source of low-redshift dispersion measurements for comparison. For the SAMI galaxies, we use R_e measured from the $H\alpha$ emission line (SAMI DR3; Croom et al. 2021) as discussed for MAGPI galaxies in Section 2.1.1, and dust-corrected $H\alpha$ -based SFRs (Kennicutt 1998), using the dust extinction law of Cardelli et al. (1989), for better comparisons. We note that Varidel et al. (2020) used R_e measured using r -band images (Bryant et al. 2015) and SFRs measured by MAGPHYS (da Cunha et al. 2008) using full spectral energy distribution fits to 21 photometric bands spanning the UV, optical and far-infrared.

2.3 KROSS

The KMOSS Redshift One Spectroscopic Survey (KROSS; Stott et al. 2016) observed 795 star-forming galaxies at $z=0.8$ – 1.0 using the K -band Multi Object Spectrograph (KMOS; Sharples et al. 2013) on the VLT. Each IFU of KMOS covers a $2.8'' \times 2.8''$ field with $0.2'' \times 0.2''$ spatial pixels. The $H\alpha$ line in this redshift range is observed within the YJ -band grating with spectral resolution $R = 3400$. We use R_e measured from the $H\alpha$ flux.

Varidel et al. (in prep)² measure the gas velocity dispersion of 315 KROSS galaxies using BLOBBY3D. They remove AGN galaxies and highly-inclined galaxies ($i > 60^\circ$) and galaxies where the mode of the gas velocity dispersion in the posterior distribution is smaller than the thermal contribution of the gas, 9 km s^{-1} (which might be caused by the variation in spectral resolution on KMOS). They also removed major mergers, i.e. galaxies with clearly disturbed kinematics. This leaves 193 galaxies for further analysis.

We use the redshift, SFR, stellar mass, and inclination angle from the publicly available KROSS catalogue (Harrison et al. 2017). The SFRs are calculated using the integrated $H\alpha$ luminosity with dust extinction applied (Wuyts et al. 2011). Stellar masses are estimated by scaling the H -band AB magnitude by a constant mass-to-light ratio for all galaxies, assuming a Chabrier (2003) IMF. Harrison et al. (2017) adopted the median mass-to-light ratio for the KROSS sample, $\gamma_H = 0.2$.

We show the SFR- M_* relation for SAMI, MAGPI and KROSS galaxies in our sample in Figure 1(a). This shows that galaxies in the MAGPI sample have similar mass and SFR distribution, while the galaxies in the KROSS sample have higher mass and SFR. The MAGPI galaxies that have $H\alpha$ -based SFR measurement but that are not in our final sample are shown as grey circles. In Figure 1(b), we show the sSFR as a function of redshift for galaxies in the surveys. The evolution of sSFR of the galaxies in our sample aligns with the result in Popesso et al. (2023), which captured the evolution of the star formation main sequence (SFMS).

² This work has been published in PhD thesis: <https://hdl.handle.net/2123/25670>

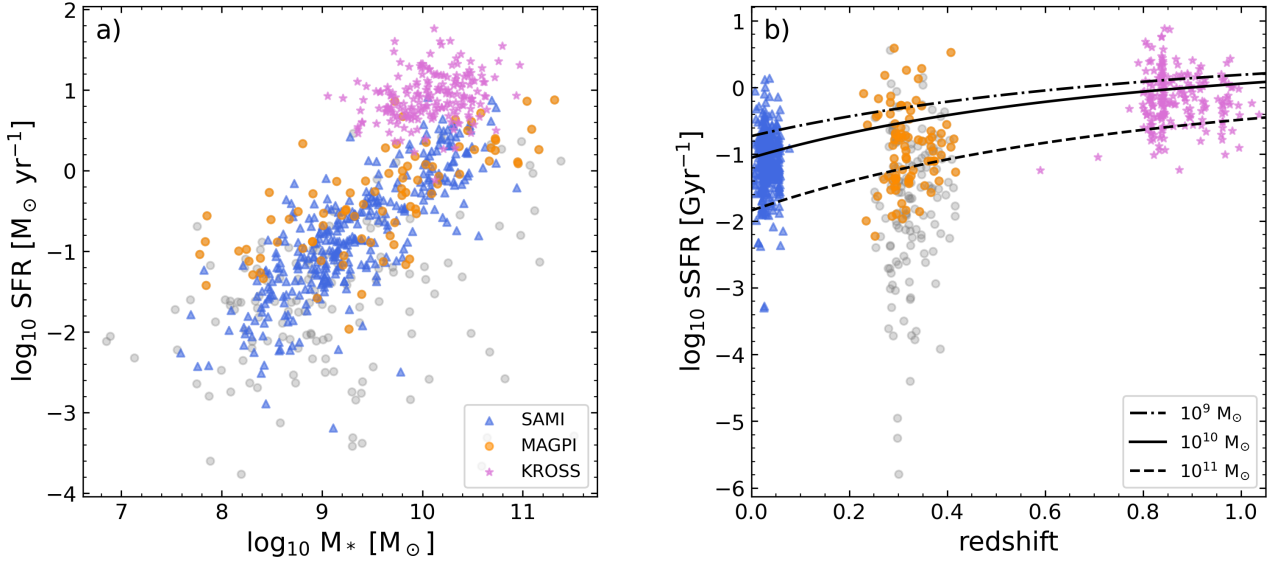


Figure 1. a) The SFR- M_* relation for SAMI (blue), MAGPI (orange) and KROSS (purple) galaxies in our sample. MAGPI galaxies that have $H\alpha$ -based SFR measurement but that are not in our final sample are shown in grey. b) The sSFR-redshift relation for galaxies in our sample. The black lines show the evolution of sSFR as a function of redshift drawn from [Popesso et al. \(2023\)](#) at three stellar mass values: 10^9 (dot-dashed line), 10^{10} (solid line) and $10^{11} M_\odot$ (dashed line).

3 METHODS

3.1 Modeling the gas disc kinematics

We use the forward-modelling technique, `BLOBBY3D`³ ([Varidel et al. 2019](#)), to infer the spatial distribution and kinematics of the gas simultaneously. `BLOBBY3D` is a Bayesian inference code for gas disc kinematics, using a Gaussian mixture model for the spatial distribution of the gas but assuming a thin regularly rotating galaxy. `BLOBBY3D` does not impose a specific spatial gas structure, but instead decomposes the gas distribution into a sum of positive-definite Gaussian basis functions (blobs), which gives it more flexibility in modelling the gas distribution. `BLOBBY3D` constructs a 3D (position-position-wavelength) cube that is convolved by the PSF in the spatial direction and the LSF in the wavelength direction. The convolved model is compared to the observed data cube. `BLOBBY3D` uses a diffusive nested sampling algorithm ([Skilling 2004](#)), `DNest4` ([Brewer et al. 2011; Brewer & Foreman-Mackey 2018](#)), to run Markov Chain Monte Carlo (MCMC) chains to explore the posterior distribution. The advantage of `DNest4` over other sampling algorithms is in its application to high dimensional parameter spaces and multimodal distributions, which is essential to model the gas distribution and kinematics of galaxies. `DNest4` allows `BLOBBY3D` to jump to different models with varying numbers of blobs. For all parameters fitted in `BLOBBY3D`, see more details in Table 1 of [Varidel et al. \(2019\)](#). The results we use in this work are the median value over the gas velocity dispersion in the posterior samples.

We measure the ionised gas velocity dispersion of MAGPI galaxies using the $H\alpha$ emission line. An example set of 2D maps, showing the results of using `BLOBBY3D` on a MAGPI galaxy 1506106169, is displayed in Figure 2. This galaxy is a median-size galaxy in our sample, which has 329 spaxels with $H\alpha$ S/N greater than 3.

3.1.1 Velocity profile

`BLOBBY3D` assumes a continuous velocity profile for the galaxy, based on an empirical model proposed by [Courteau \(1997\)](#)

$$v(r) = v_c \frac{(1 + r_t/r)^\beta}{(1 + (r_t/r)^\gamma)^{1/\gamma}} \sin(i) \cos(\theta) + v_{\text{sys}}, \quad (1)$$

where v_c is the asymptotic velocity, r is the distance to the kinematic centre, r_t is the turnover radius, β is a parameter that controls the gradient of the velocity profile, γ is a parameter that controls the sharpness of the velocity profile turnover point, v_{sys} is a systemic velocity term, i is the inclination of the galaxy and θ is the polar angle in the plane of the disc. We calculate inclinations from the axis ratio (b/a) of the white-light image of MAGPI MUSE data, which are estimated using the tool `PROFOUND` ([Robotham et al. 2018](#)), as

$$\cos(i) = \sqrt{\frac{(b/a)^2 - q_0^2}{1 - q_0^2}}, \quad (2)$$

where q_0 is the intrinsic axial ratio of an edge-on galaxy ([Weijmans et al. 2014](#)); here we adopt $q_0 = 0.2$, following [Cortese et al. \(2016\)](#). We note that the adopted value of q_0 may influence the estimation of v_c , but the fit gas velocity dispersion is insensitive to q_0 . The emission line broadening caused by beam smearing is related to line-of-sight velocity, which is the combination of inclination and rotational velocity. Therefore, the underestimation or overestimation of i can be balanced by v_c in Eq. 1.

3.1.2 Velocity dispersion gradient

`BLOBBY3D` allows flexibility to assume different forms for the velocity dispersion as a function of radius. We adopt a flat velocity dispersion profile to simplify the inference following [Varidel et al. \(2020\)](#)'s analysis for SAMI galaxies. However, other surveys have shown that velocity dispersion can be radially variant (e.g. [Genzel et al. 2017; Yu et al. 2019](#)). We therefore tested using a log-linear profile and

³ <https://github.com/SpaceOdyssey/blobby3d>

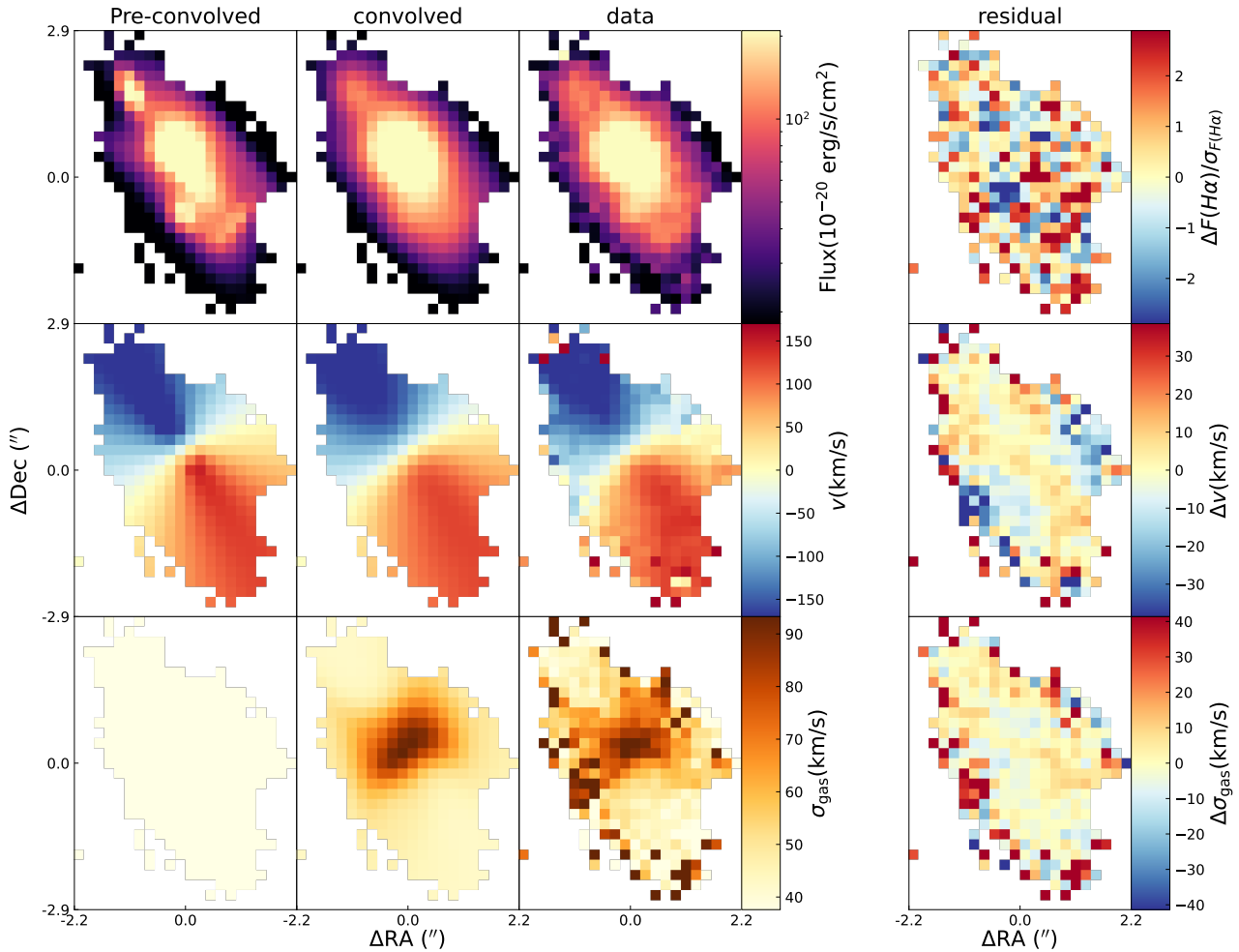


Figure 2. The 2D maps of the `BLOBBY3D` results for MAGPI galaxy 1506106169. The first column shows the model made by `BLOBBY3D`; the second column shows the model convolved with the PSF and LSF of the data; the third column shows the results of the single Gaussian fit to the observed datacube; the fourth column shows the residuals between the data and the convolved model. The first row shows the flux distribution of the $H\alpha$ emission line; the second row shows the velocity map; the third row shows the velocity dispersion map.

fit all spaxels with $S/N > 3$ in $H\alpha$. We have 11 AGN-host galaxies in our preliminary sample. These galaxies tend to have a higher central velocity dispersion, which forces a steep velocity dispersion slope and leads to an under-estimate of the outer dispersion. For this reason, we mask central AGN regions based on the BPT maps (Kewley et al. 2001; Kauffmann et al. 2003). We note that the small number of high-dispersion pixels at the edges of the velocity maps in some galaxies (as seen in Figure 2) are likely spurious artifacts caused by low $H\alpha$ S/N in these regions. This was also the case in the Varidel et al. (2020) analysis for SAMI galaxies.

For comparison, we run the model fits using both a constant velocity dispersion across the entire galaxy and a gradient in the dispersion. Overall, we find flat gradients and mean velocity dispersions that do not change significantly across the galaxies in either fit. We therefore choose the simpler constant velocity dispersion model.

4 RESULTS

4.1 Velocity dispersions of MAGPI galaxies

Of 110 selected galaxies in our preliminary sample, 87 have a unimodal posterior distribution in gas velocity dispersion (σ_{gas}) with a peak at a realistic velocity (i.e. $> 10 \text{ km s}^{-1}$). The mode of the posterior distribution of the remaining 23 galaxies is at 0 km s^{-1} , which is unrealistic. This may result from an intrinsic dispersion much lower than the spectral resolution of MUSE, which `BLOBBY3D` is not able to resolve. The galaxies that do not have reliable velocity dispersion fits have low SFR and low gas velocity dispersion, and typically have large uncertainties in gas velocity dispersion. For those galaxies without reliable fit, the 95 percentile of σ_{gas} of posterior samples is taken as the upper limit.

The average σ_{gas} for the 87 MAGPI galaxies that have reliable fit is $26.1 \pm 8.7 \text{ km s}^{-1}$, where $\pm 8.7 \text{ km s}^{-1}$ represents the standard deviation. When we include the upper limit of σ_{gas} for galaxies without reliable fits, the average σ_{gas} for the 110 galaxies is $23.4 \pm 9.8 \text{ km s}^{-1}$. Figure 3 shows SFR versus gas velocity dispersion for 110 MAGPI galaxies, colour-coded by stellar mass. This includes 76 star-forming galaxies (circles) and 11 AGN-host galaxies (stars). The

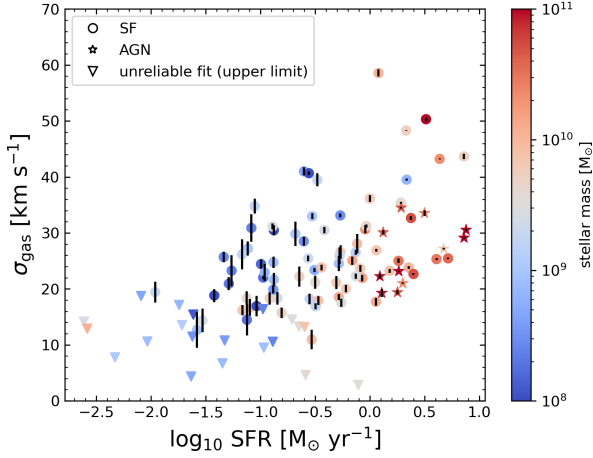


Figure 3. The intrinsic gas velocity dispersion of MAGPI galaxies measured by BLOBBY3D as a function of SFR, colour-coded by stellar mass. Star-forming galaxies are shown as circles and galaxies with AGN at the centre are shown as stars. The upper limits of σ_{gas} for galaxies without reliable fits are shown as downward triangles. The black errorbars show the uncertainties on σ_{gas} .

standard deviations of the posterior effective samples are shown as error bars. We show the upper limits of σ_{gas} for galaxies without a reliable fit (downward triangles). Note that we remove those galaxies with unreliable fits from any further analysis.

The spectral resolution for the $\text{H}\alpha$ line of MAGPI galaxies corresponds to $\sim 38 \text{ km s}^{-1}$. The minimum velocity dispersion that converges in the galaxies we selected is 11.0 km s^{-1} , about 1/3 of the instrumental resolution. It is difficult to measure the intrinsic velocity dispersion if it is much lower than the instrumental resolution (Wisnioski et al. in prep).

Most of the galaxies with AGN sit at high SFR in Figure 3. These galaxies also have larger sizes and higher stellar masses (see Section 4.2), which are positively correlated with SFR. However, it is noteworthy that they tend to have lower dispersion than other galaxies of the same SFR. We test whether the masking of the centres of the AGN galaxies influences our measurements by selecting 9 SF galaxies, masking their centres and then refitting for σ_{gas} . This test shows that the differences of σ_{gas} between the centre-masked and no-mask versions are a few km s^{-1} and the average offset is 0.4 km s^{-1} . This suggests that our approach of masking the central region in AGN-host galaxies does not bias the σ_{gas} measurements.

Galaxies with AGN at the centre do not have higher dispersion than the galaxies with similar SFR, which indicates that the AGN in our sample, though they may have high gas velocity dispersion in the central AGN region, do not influence the global gas velocity dispersion of the star-forming disc of their host galaxies. AGN-host galaxies are closer to the average values of dispersion at fixed Σ_{SFR} (see Section 4.2 below).

4.2 Correlations between velocity dispersion and other galaxy properties

To investigate what factors can impact gas velocity dispersion, we calculate the Pearson correlation coefficient (r) between gas velocity dispersion and galaxy properties, such as total SFR, specific SFR (sSFR), Σ_{SFR} , stellar mass, R_e , a proxy for the gravitational potential (M_*/R_e), Σ_{M_*} , and the logarithmic offset in SFR from the SFMS of MAGPI galaxies (ΔSFR). The SFMS is defined as the best linear fit

to the MAGPI galaxies located at $0.25 \leq z \leq 0.424$ that have SFRs measured from $\text{H}\alpha$ (Mun et al. 2024). We plot all these correlations in Figure 4, with the Pearson correlation coefficient (r) and p -value on each plot. The Pearson correlation coefficient measures the linear correlation between two variables. The p -value helps determine whether the observed correlation is statistically significant. A p -value of 0.05 or lower is generally considered statistically significant.

We find that the gas velocity dispersion of MAGPI galaxies is strongly correlated with SFR, as already shown in Figure 3, with correlation coefficient $r = 0.46$. We look at properties derived using SFR to see if they reduce the scatter in the $\sigma_{\text{gas}} - \text{SFR}$ relation. When SFR is combined with R_e , the Σ_{SFR} gives a stronger correlation with σ_{gas} ($r = 0.65$) than SFR, while R_e has no significant correlation with σ_{gas} ($r = -0.17$). This result is consistent with galaxies at $z \sim 0.05$ (SAMI; Varidel et al. 2020). This trend may arise from star-formation feedback, mainly from the supernova, which injects energy into neighbouring gas, leading to turbulence and increasing the gas velocity dispersion (e.g. Faucher-Giguère et al. 2013; Krumholz et al. 2018). The rate of energy injection per unit area, traced by Σ_{SFR} , is more correlated with gas velocity dispersion than the global SFR of galaxies, which indicates that the star formation on small scales within the disc may be more important than the global SFR of the galaxy.

We also calculate the $\Sigma_{\text{SFR},i\text{-band}}$ using $R_{e,i\text{-band}}$ ($\Sigma_{\text{SFR},i\text{-band}} = \text{SFR}/(2\pi R_{e,i\text{-band}}^2)$). The $R_{e,i\text{-band}}$ is the half-light radius of i -band image of MAGPI galaxies that is estimated by fitting a single Sérsic profile using Galfit (Peng et al. 2010). We find that the Σ_{SFR} using R_e of the $\text{H}\alpha$ flux gives a higher correlation coefficient ($r = 0.65$) than $\Sigma_{\text{SFR},i\text{-band}}$ ($r = 0.61$). As we might expect, Σ_{SFR} calculated by $\text{H}\alpha$ R_e has a tighter correlation, because it more accurately portrays the Σ_{SFR} of star-forming regions within the galaxies.

We incorporate SFR with stellar mass in two different ways, i.e. sSFR and ΔSFR . ΔSFR has a slightly stronger correlation ($r = 0.50$) with σ_{gas} than SFR. sSFR does not reduce the scatter in $\sigma_{\text{gas}} - \text{SFR}$ relation, with $r = 0.37$ for sSFR. Also, we find that M_* have no significant correlation with σ_{gas} ($r = 0.09$). There is no significant correlation between σ_{gas} and M_*/R_e ($r = 0.16$), in contrast to stellar velocity dispersion correlating with potential, which indicates that the gas velocity dispersion is more easily influenced by local power sources (Oh et al. 2022). We note that $M_*/R_{e,i\text{-band}}$ is a better proxy for gravitational potential, but the correlation coefficient does not change when we use $M_*/R_{e,i\text{-band}}$. We use $\text{H}\alpha$ R_e for all parameters in Figure 4 for consistency. Σ_{M_*} is weakly correlated with σ_{gas} ($r = 0.24$).

From the galaxy SFMS, we know that galaxies with higher mass tend to have higher SFR. To disentangle the correlation between these parameters, we carry out a partial correlation analysis as shown in Figure 5 using PINGOUIN (Vallat 2018). Partial correlation measures the correlation between two variables, with the effect of other variables removed. The partial correlations between σ_{gas} , SFR, M_* and R_e show that SFR has the strongest correlation with σ_{gas} ($r = 0.598$) when we take M_* and R_e into account. M_* has no significant partial correlation with σ_{gas} ($r = -0.1$). Though no significant correlation has been found between σ_{gas} and R_e in Figure 4, R_e has a negative partial correlation with σ_{gas} ($r = -0.407$), indicating that SFR and galaxy size have a combined effect on gas velocity dispersion. It provides further evidence that Σ_{SFR} is more important than total SFR on σ_{gas} , as demonstrated in Figure 4.

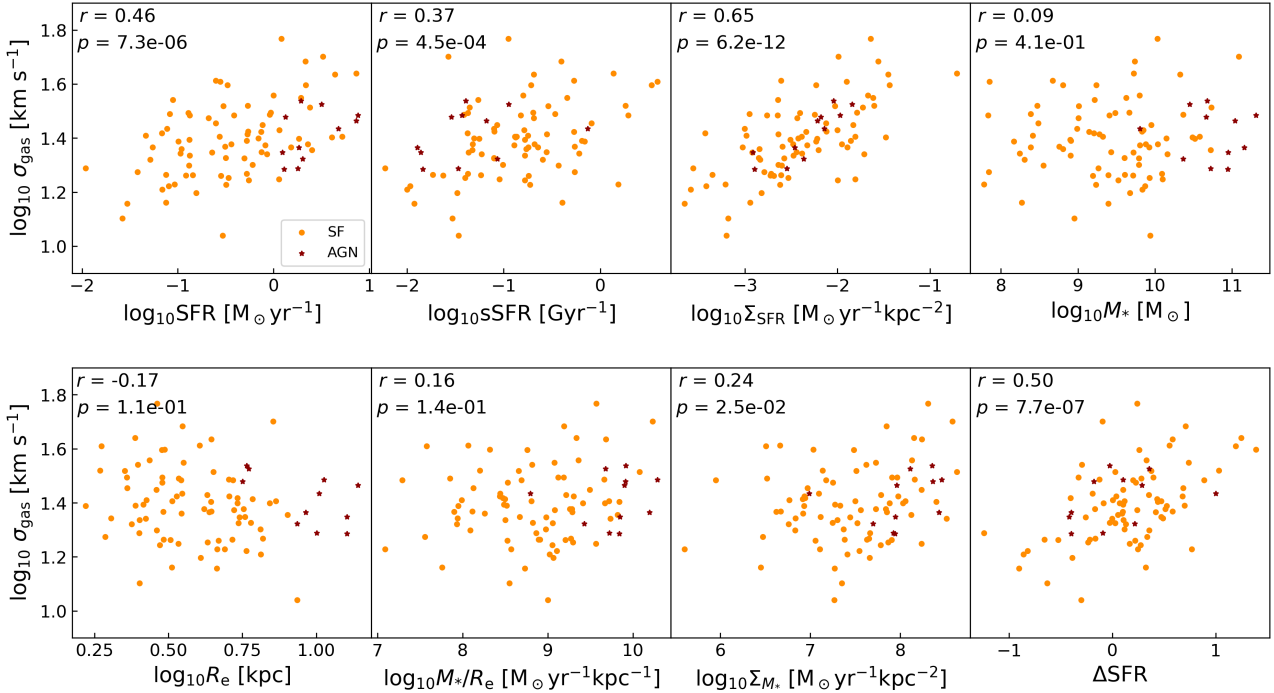


Figure 4. Intrinsic gas velocity dispersion (σ_{gas}) as a function of galaxy properties for MAGPI galaxies, including star-forming rate (SFR), specific star-formation rate (sSFR), star-formation rate surface density (Σ_{SFR}), stellar mass (M_*), half-light radius of H α flux (R_e), a proxy for the gravitational potential (M_*/R_e), stellar mass surface density (Σ_{M_*}), and the logarithmic offset in SFR from the star formation main sequence of MAGPI galaxies (ΔSFR). Pearson correlation coefficient, r , and p -value for each correlation are shown on each panel. The star-forming galaxies are shown as orange circles and the AGN-host galaxies are shown as dark red stars. We find the σ_{gas} of MAGPI galaxies has the strongest correlation with Σ_{SFR} ($r = 0.65$). The σ_{gas} also has a strong correlation with SFR and ΔSFR .

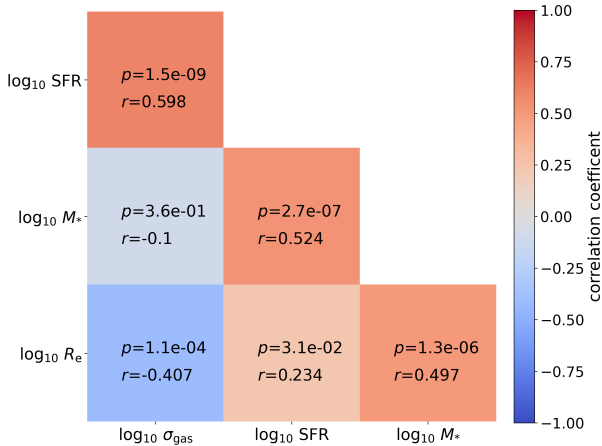


Figure 5. The partial correlations between gas velocity dispersion, SFR, M_* and R_e for the MAGPI sample. The Pearson correlation coefficient (r) and p -value are given in each box, which is colour-coded by its correlation coefficient. The partial correlation shows that SFR still has a strong correlation with gas velocity dispersion ($r = 0.598$) when we remove the effects from M_* and R_e . R_e has a negative partial correlation with σ_{gas} ($r = -0.407$), indicating that SFR and galaxy size have a combined effect on gas velocity dispersion.

4.3 Non-rotational gas velocities

We also want to investigate other mechanisms that might influence gas turbulence, such as gas accretion and gas transportation through a disc. We use the velocity residual between the observed MAGPI

velocity map, derived using single Gaussian component fit, and the convolved model as an indicator of non-regular rotational velocity. The model velocity profile in BLOBBY3D only contains rotation. Therefore, the deviation of the observed velocity map from the model velocity map can be considered as non-rotational motion (or at least deviations from regular rotation). We calculate the average velocity residual (Δv) weighted by H α line S/N of each spaxel to reduce the impact of the low S/N spaxels at the edge of galaxy, as follows:

$$\Delta v = \frac{\sum_{i \in \Omega} |v_{\text{con}} - v_{\text{data}}|_i \cdot sn_i}{\sum_{i \in \Omega} sn_i}, \quad (3)$$

where Ω includes all spaxels with H α S/N greater than 10, v_{con} is the velocity in the convolved model of each spaxel, v_{data} is the velocity in the data, sn is the S/N of each spaxel. Then we investigate its correlation with gas velocity dispersion.

Since the $\sigma_{\text{gas}} - \Sigma_{\text{SFR}}$ is the strongest correlation we find ($r = 0.65$), we colour-coded the galaxies in our sample in the $\sigma_{\text{gas}} - \Sigma_{\text{SFR}}$ plane by their average velocity residual (shown in Figure 6a), to see whether non-rotational velocity contributes to the scatter of this relation. The dashed line in Figure 6a is fitted by ordinary least squares regression. We find that the galaxies above the line tend to have slightly (but non-negligible) higher velocity residuals. The average velocity residual is $4.54 \pm 0.28 \text{ km s}^{-1}$ for the galaxies above the line and is $3.67 \pm 0.16 \text{ km s}^{-1}$ for the galaxies under the line. The velocity residual difference is small compared to the rotational velocity of the galaxy ($\sim 100 \text{ km s}^{-1}$). When we look at the large-scale velocity residual in individual galaxies, the velocity residual in some regions could be up to $\sim 40 \text{ km s}^{-1}$ (e.g. see Figure 10 below).

We further investigate the partial correlation between σ_{gas} , Σ_{SFR} , Δv and M_* , as shown in Figure 6b. The correlation coefficient be-

tween σ_{gas} and Σ_{SFR} is $r = 0.71$. The correlation coefficient between σ_{gas} and Δv is $r = 0.424$. The result shows that in addition to Σ_{SFR} , our measurement of gas velocity dispersion may also be related to non-circular motions of the gas. We test an alternative method to find asymmetry, by rotating the seeing convolved velocity map by 180° , but this approach has more noise (the velocity residuals are consistently larger), likely because a non-uniform flux distribution plus beam smearing can generate kinematic asymmetries. This method reduces the significance of the signal we see, but we do not consider it reliable.

Among all MAGPI galaxies in our sample, we find that four galaxies with high Δv show an interesting Fourier $m = 3$ pattern in the velocity residual maps. We will further discuss this in Section 5.2.

4.4 Comparison to the SAMI and KROSS surveys

We compare the MAGPI sample with the SAMI ($z \sim 0.05$) and KROSS ($z \sim 1$) samples, of which the σ_{gas} is measured in a consistent method. As the SAMI and KROSS samples only include SF galaxies, we remove the AGN-host galaxies from our MAGPI sample in the following comparison. We note that removing AGN-host galaxies does not change our results. Figure 7 compares the MAGPI, SAMI and KROSS velocity dispersions against several other galaxy properties. The Pearson correlation coefficients, r , and the p -values are shown for each survey separately. The histograms illustrate that the distribution of galaxy properties of MAGPI and SAMI galaxies are similar, although MAGPI galaxies have slightly higher stellar mass and higher SFR than SAMI galaxies. KROSS galaxies have ~ 2 dex higher SFR and ~ 1 dex higher stellar mass.

We find that both MAGPI and SAMI data show that σ_{gas} is strongly correlated with SFR and Σ_{SFR} . Also, both MAGPI and SAMI data show that Σ_{SFR} has a higher correlation coefficient than SFR, which may indicate that higher energy injection per unit area by star-formation feedback, rather than total SFR of the galaxy, drives higher σ_{gas} . We also find ΔSFR has a strong correlation ($r \sim 0.5$) with σ_{gas} for SAMI and MAGPI galaxies.

Similar to Figure 5, the partial correlations between σ_{gas} , SFR, M_* and R_e for SAMI galaxies show that there is no partial correlation between σ_{gas} and M_* , indicating that the relation between stellar mass and dispersion is driven by SFR for SAMI galaxies. There is no partial correlation between σ_{gas} and M_* for KROSS galaxies. The progenitors of SAMI galaxies, at the redshifts of MAGPI and KROSS, will have lower stellar masses. However, the stellar mass has no partial correlation with σ_{gas} for SAMI, MAGPI and KROSS galaxies, indicating that mass-related progenitor bias is unlikely to be significant for our σ_{gas} analysis.

Interestingly, although there is no correlation between σ_{gas} and SFR found for KROSS galaxies, there is a significant correlation between σ_{gas} and Σ_{SFR} . This result suggests Σ_{SFR} is also more important than SFR for high redshift galaxies. However, we note that the range of SFR for KROSS galaxies is narrower (on a log-scale) than SAMI and MAGPI, which limits our ability to detect a correlation.

As Σ_{SFR} has the strongest correlation with σ_{gas} for MAGPI and SAMI galaxies, and a moderate correlation with KROSS galaxies, we calculate the average σ_{gas} in each 0.5 dex bin for MAGPI, SAMI and KROSS galaxies separately. Figure 8 shows that the average σ_{gas} is similar for SAMI, MAGPI and KROSS galaxies at the fixed Σ_{SFR} and the average σ_{gas} lines up for galaxies from three surveys at different redshifts, which may suggest that the mechanism that relates to Σ_{SFR} is the main driver of gas turbulence at different redshifts.

5 DISCUSSION

5.1 Gas velocity dispersion evolution through cosmic time

We show the intrinsic gas velocity dispersion of SAMI, MAGPI and KROSS galaxies as a function of lookback time (t_{lookback}) in Figure 9. The velocity dispersion of these galaxies is all measured using BLOBBY3D. Previous observational studies have shown gas velocity dispersion decreases with cosmic time, so that galaxies have higher gas velocity dispersion when the Universe was younger (Kassin et al. 2012; Wisnioski et al. 2015; Übler et al. 2019). With the addition of the MAGPI data, a large IFS dataset at this epoch, we can explore the different mechanisms which may drive turbulence and their evolution.

Two versions of the ordinary linear regression fitting of the gas velocity dispersions of SAMI, MAGPI and KROSS galaxies are shown in Figure 9. The linear relation between gas velocity dispersion and lookback time (line 1) is shown as a black solid line and is given by

$$\sigma_{\text{gas}}[\text{km s}^{-1}] = 3.4(\pm 0.2) \cdot t_{\text{lookback}} + 20.1(\pm 0.8) . \quad (4)$$

The relation between gas velocity dispersion and redshift (line 2) is shown as a black dot-dash line and is given by

$$\sigma_{\text{gas}}[\text{km s}^{-1}] = 27.5(\pm 1.4) \cdot z + 21.0(\pm 0.7) . \quad (5)$$

Our results show a decreasing trend of gas velocity dispersion from $z = 1$ to $z = 0$, which is consistent with previous studies. Both Wisnioski et al. (2015) and Übler et al. (2019) showed clear decreasing trends of gas velocity dispersion over cosmic time using data of KMOS^{3D} in the redshift range $0.6 < z < 2.6$. Übler et al. (2019) did a linear regression of gas velocity dispersion and redshift using the gas velocity dispersion of KMOS^{3D} galaxies and ionised gas velocity dispersion from the literature at $0 < z < 4$. The fit in Übler et al. (2019) is described by the equation

$$\sigma_{\text{gas}}[\text{km s}^{-1}] = 9.8(\pm 3.5) \cdot z + 23.3(\pm 4.9) . \quad (6)$$

The gas velocity dispersion of SAMI, MAGPI and KROSS in our results are consistent with $\sigma_{\text{gas}} - z$ linear fitting in Übler et al. (2019). The gas velocity dispersion of MAGPI galaxies at $z \sim 0.3$ is in good agreement with the results in the slit based DEEP2 survey (Kassin et al. 2012). The average velocity dispersion of KROSS galaxies measured with BLOBBY3D agrees with Johnson et al. (2018), who measured the gas velocity dispersion of KROSS galaxies fitting a single Gaussian component with beam smearing correction applied. The KROSS galaxies at $z \sim 1$ have higher gas velocity dispersion than the KMOS^{3D} galaxies at a similar redshift. This difference may be due to differences in sample selection; Übler et al. (2019) applied strict criteria to select only settled-disc galaxies, which may exclude the most turbulent galaxies and thus lower the average gas dispersion of the sample. We remark that we did not apply the strict selection criteria of Übler et al. (2019) to our sample of KROSS galaxies, but we removed galaxies with clear indications of ongoing major mergers.

The evolution of gas velocity dispersion fits in a consistent picture with the evolution of star formation and gas fraction. Previous studies have found that the sSFR decreases over cosmic time (Madau et al. 1998; Hopkins & Beacom 2006; Madau & Dickinson 2014; Leslie et al. 2020; Popesso et al. 2023). The decreasing global averages of gas velocity dispersion is consistent with decreasing sSFR, which is an important galaxy property that correlates with gas velocity dispersion. The evolution in sSFR is fairly flat from $z \sim 5$ to $z \sim 1$, only slightly decreasing. Most of the change appears to have happened between $z \sim 1$ to 0. Galaxy gas content, which is the fuel of star formation, also evolves with cosmic time. Star-forming

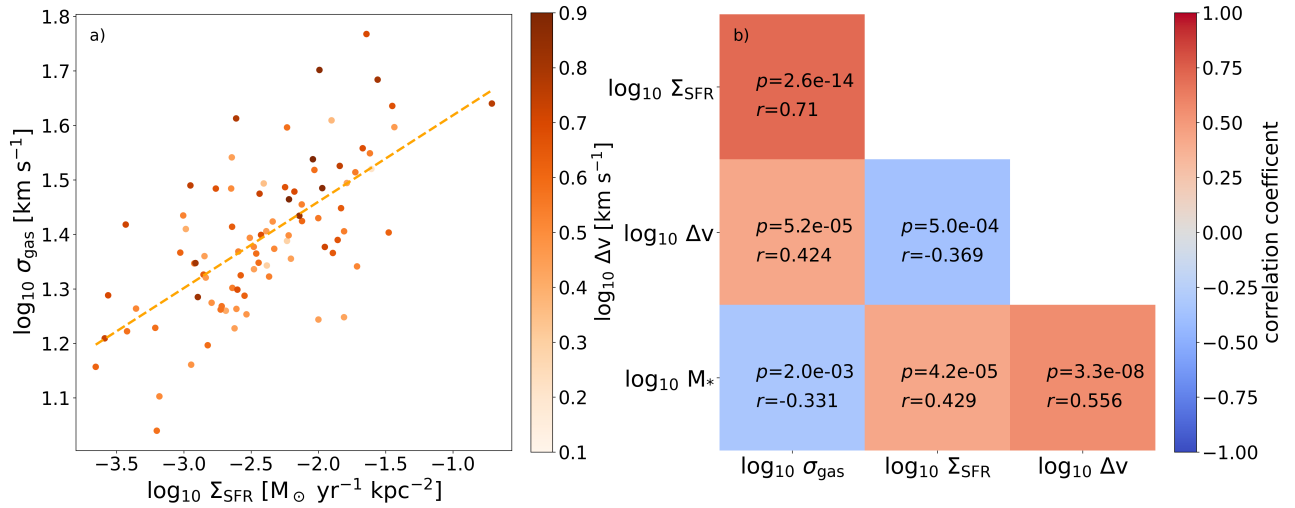


Figure 6. a) Gas velocity dispersion versus Σ_{SFR} colour-coded by average velocity residual (Δv). The dashed line is the ordinary least squares regression line. b) The Pearson partial correlation between σ_{gas} , Σ_{SFR} , Δv and M_{*} . The Pearson correlation coefficient (r) and p -value are shown in each box, which is colour-coded by correlation coefficient. The result shows that in addition to Σ_{SFR} , gas velocity dispersion may also be related to non-circular motions of the gas.

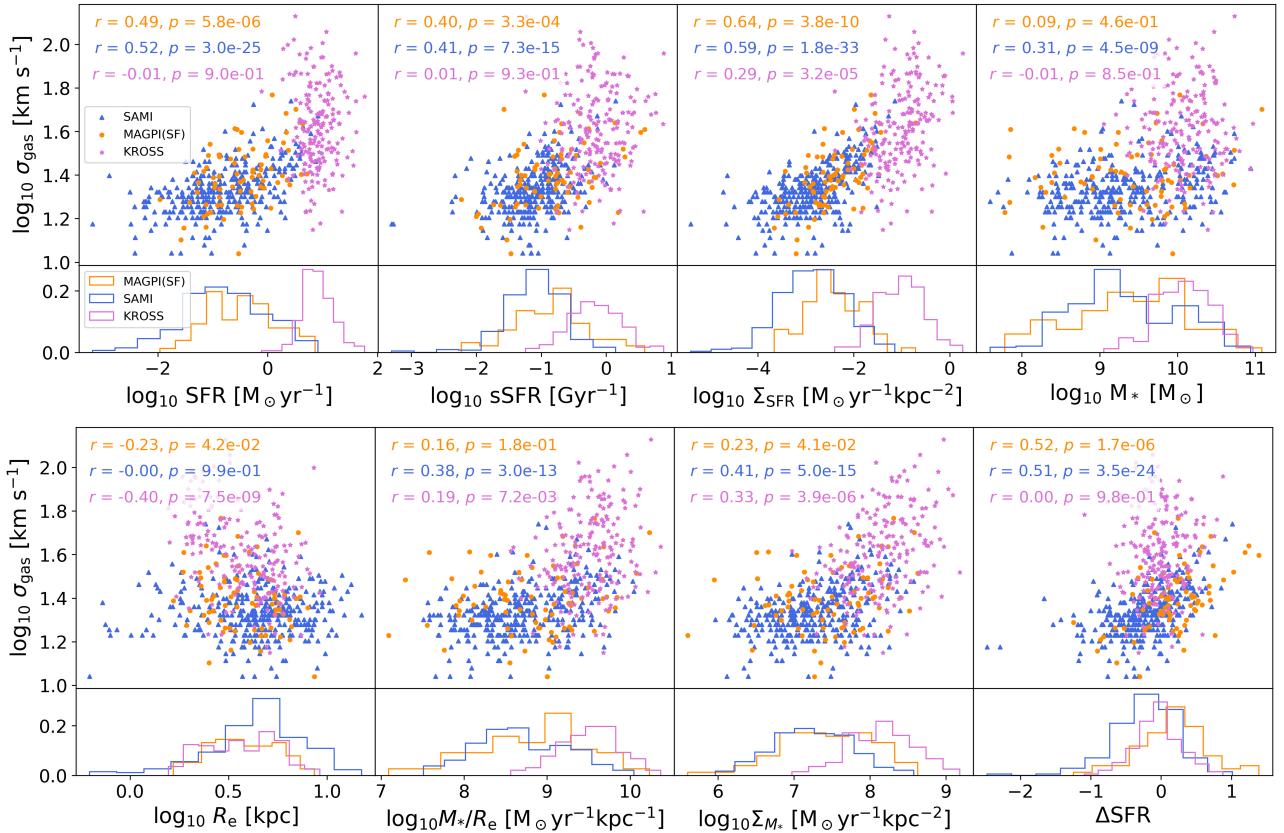


Figure 7. The relationship between gas velocity dispersion and galaxy properties for MAGPI (orange), SAMI (blue) and KROSS (purple) survey. The lower panel of each plot shows the distribution of galaxy properties. The Pearson correlation coefficients (r) and p -values are shown on each plot. Both MAGPI and SAMI galaxies have the strongest correlation between σ_{gas} and Σ_{SFR} . KROSS galaxies also have a modest correlation between σ_{gas} and Σ_{SFR} .

galaxies in earlier cosmic epochs held more molecular gas compared to the present time (e.g. Tacconi et al. 2020). The gas fractions of star-forming galaxies have decreased from $z = 3$ to $z = 0$ at a roughly constant rate (Wiklind et al. 2019).

5.2 Drivers of gas turbulence

We discussed the correlation between SFR and σ_{gas} ($r = 0.46$) and between Σ_{SFR} and σ_{gas} ($r = 0.65$) for MAGPI galaxies in Section 4.2. There is also a strong correlation between Σ_{SFR} and σ_{gas} for

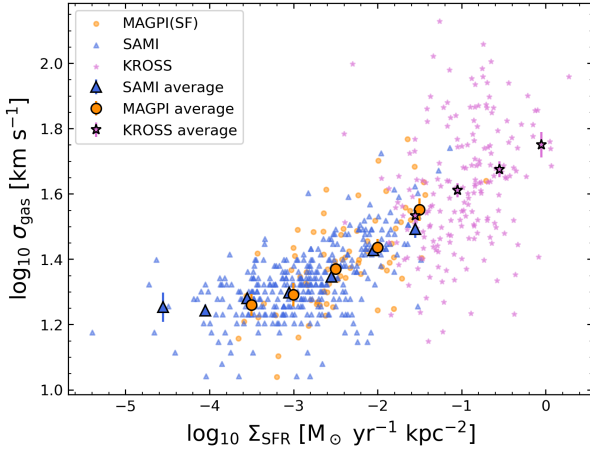


Figure 8. The $\sigma_{\text{gas}} - \Sigma_{\text{SFR}}$ relation for MAGPI (orange), SAMI (blue) and KROSS (purple) galaxies. The average σ_{gas} in each 0.5 dex bin for SAMI, MAGPI and KROSS are shown as black-edge triangles, circles and stars. The errorbars show the standard error of the mean.

SAMI galaxies and a moderate correlation for KROSS galaxies. The average σ_{gas} is similar for SAMI, MAGPI and KROSS galaxies at the fixed Σ_{SFR} , as shown in Figure 8.

Star-formation feedback is considered to be an important source of gas turbulence since it injects energy into the interstellar medium (Ostriker & Shetty 2011; Shetty & Ostriker 2012; Faucher-Giguère et al. 2013; Krumholz & Burkhardt 2016; Krumholz et al. 2018; Bacchini et al. 2020; Sun et al. 2020; Ceverino et al. 2017). Some analytical models and theories proposed that the energy from star-formation feedback sweeps up gas, then the shell of gas breaks up and merges with the interstellar medium, generating turbulence. The rate of energy injection per unit area, which is determined by the momentum injected per unit mass, star-formation surface density and gas velocity dispersion, balances the energy loss rate by turbulent dissipation (Krumholz et al. 2018; Faucher-Giguère et al. 2013; Krumholz et al. 2017). Given the importance of stellar feedback on driving turbulence, we expect a positive correlation between gas velocity dispersion and Σ_{SFR} .

The strong correlations between σ_{gas} and SFR, and between σ_{gas} and Σ_{SFR} have been observed by many observational studies (Green et al. 2010; Lehnert et al. 2013; Green et al. 2014; Moiseev et al. 2015b; Zhou et al. 2017; Johnson et al. 2018; Yu et al. 2019; Varidel et al. 2020; Law et al. 2022) and simulation studies (Shetty & Ostriker 2012; Hung et al. 2019; Jiménez et al. 2023; Rathjen et al. 2023), that can be considered as the evidence of star-formation feedback driving gas turbulence. In particular, Egorov et al. (2023) using high-resolution observations of gas superbubbles, showed a dependence of the kinetic energy of ionised gas velocity dispersion on energy input from stellar feedback, which provided further support for the star-formation feedback energy injection theory.

The degree of star-formation feedback in increasing gas velocity dispersion is controversial. Some studies proposed that star-formation feedback is the dominant factor driving gas turbulence. Faucher-Giguère et al. (2013) and Bacchini et al. (2020) built theoretical models to show that star-formation feedback alone is enough to sustain gas turbulence in local and high-redshift star-forming galaxies without other energy sources. On the contrary, some studies suggested a need for additional sources of gas turbulence (Zhou et al. 2017; Bik et al. 2022; Forbes et al. 2023).

Another possible explanation for the strong correlation between

σ_{gas} and Σ_{SFR} is that gravitational instability drives gas velocity dispersion (Krumholz & Burkhardt 2016; Krumholz et al. 2018; Molina et al. 2020). The Toomre-Q parameter (Toomre 1964), or gravitational stability parameter, can be approximated by

$$Q \approx \sqrt{2} \frac{v_c \sigma_{\text{gas}} f_g}{\pi G r \Sigma_{\text{gas}}}, \quad (7)$$

where Q is the total Toomre-Q parameter for both gas and stars, v_c is the galaxy rotation curve velocity (assuming a flat rotation curve), f_g is the gas fraction, Σ_{gas} is the gas surface density. The gravitational instability creates turbulence to keep the galaxy disc in marginally stable status, i.e. $Q \approx 1$. The energy source for this mechanism is gas inward transportation through the disc. If instability arises in the disc, it will break the axisymmetry, causing the subsequent torques that drive gas inward motion until marginal stability is restored. (Bertin & Lodato 1999; Krumholz & Burkert 2010; Forbes et al. 2012, 2014; Krumholz et al. 2018). The Kennicutt-Schmidt relation shows us that Σ_{SFR} is proportional to Σ_{gas} (Kennicutt 1998; Kennicutt & Evans 2012). Therefore, the strong correlation we find between σ_{gas} and Σ_{SFR} may be a correlation between σ_{gas} and Σ_{gas} to keep the galaxy disc marginally stable, $Q \approx 1$. Further observations of f_{gas} and Σ_{gas} are needed to test this idea. For example, Krumholz & Burkhardt (2016) showed that the σ_{gas} -SFR relation is different for gravity-driven and star formation feedback-driven models. In the gravity-driven model, f_g changes the slope of the σ_{gas} -SFR relation.

Gravitational instabilities can also be induced by external influences like galaxy-galaxy interactions or accretion. In Section 4.3, we find some galaxies have large Δv values, indicating non-circular motions. Four galaxies with high Δv ($\Delta v = 8.6 \pm 2.0 \text{ km s}^{-1}$) show an interesting Fourier $m = 3$ pattern in their velocity residual maps, which means there are three approaching and three receding regions in velocity residual maps. Figure 10 shows the four MAGPI galaxies with this pattern. These galaxies are AGN-host galaxies. We mask the AGN spaxels in these galaxies. We rule out the possibility of simple gas inflows for this pattern, as the simple gas inflow model only creates an axisymmetric pattern on the line-of-sight velocity residual map (Genzel et al. 2023; Tsukui et al. 2024). The $m = 3$ patterns we see may be caused by an interaction with a satellite galaxy, which disturbs the galaxy disc and triggers the bending wave or disc corrugation, which wraps up with differential rotation (e.g. Bland-Hawthorn & Tepper-García 2021; Tepper-García et al. 2022). A warp can be also caused by misaligned gas accretion and can provide kinetic energy to gas, increasing the velocity dispersion (Khachataryants et al. 2022; Jiménez et al. 2023). One galaxy (ID=1204198199) shows evidence of interaction with neighbouring high mass galaxies in the white light image from MUSE. The other three galaxies do not have clear features indicating interactions with other galaxies, but they live in groups that might have interaction with neighbouring low-mass galaxies.

Another explanation for this $m = 3$ pattern is spiral-arm related gas flows (Kawata et al. 2014; Grand et al. 2016). Grand et al. (2016) showed that spiral arms induce large-scale streaming motion so that the gas behind the arm moves azimuthally backwards and radially outwards, while the gas at the front of the arm moves azimuthally forward and radially inward. The radial velocity in their model is $\sim 20 \text{ km s}^{-1}$ and the azimuthal velocity is $\sim 10 \text{ km s}^{-1}$ relative to the mean rotational velocity. Although the line-of-sight velocity depends on the inclination of the galaxy and the location in the galaxy, the velocity residual we find is of the same order of magnitude as the combined effect of radial and azimuthal gas flows in Grand et al. (2016). Therefore, the $m = 3$ pattern may be due to these galaxies having three spiral arms. Bland-Hawthorn et al. (2024) showed

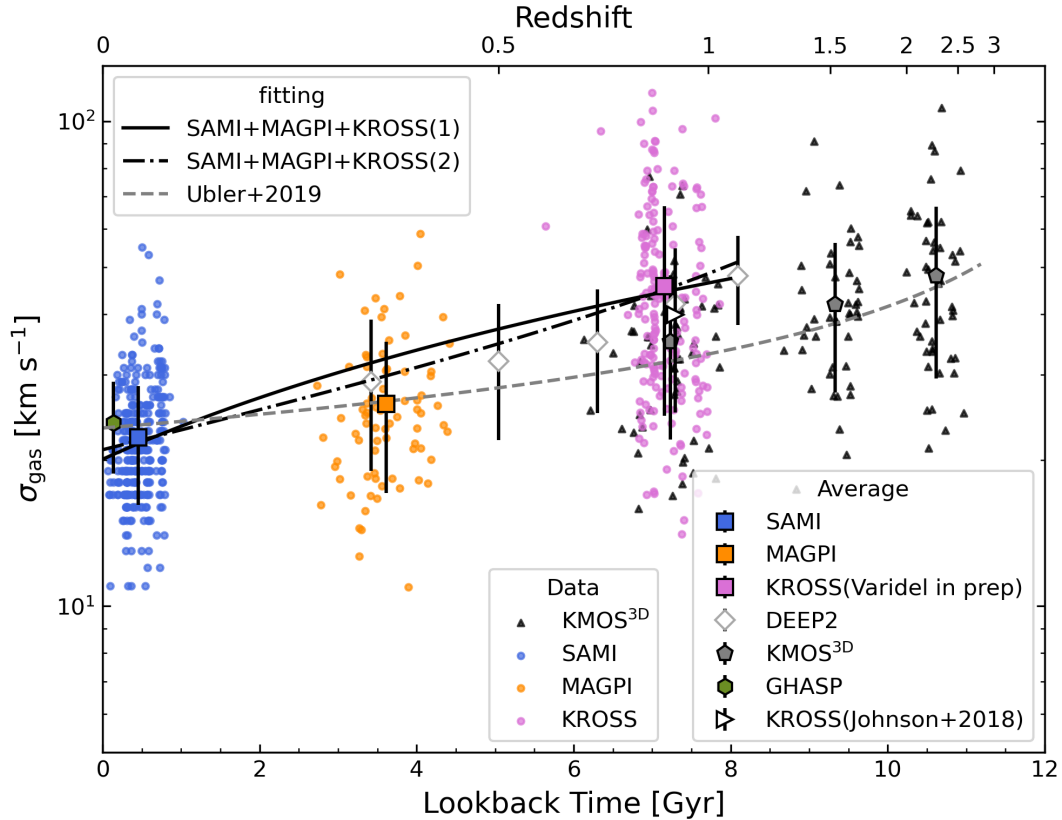


Figure 9. The gas velocity dispersion of SAMI, MAGPI and KROSS galaxies as a function of lookback time. The data from KMOS^{3D} (Übler et al. 2019) are shown as black triangles. The average σ_{gas} and the standard deviation of SAMI (Varidel et al. 2020), MAGPI, KROSS (Varidel et al. in prep), DEEP2 (Kassin et al. 2012), KMOS^{3D} (Übler et al. 2019), GHASP (Epinat et al. 2010) and KROSS (Johnson et al. 2018) are shown as different black-edge markers. The black solid line shows the ordinary linear regression between gas velocity dispersion and lookback time for the combination of SAMI, MAGPI and KROSS data, for which gas velocity dispersions are measured with the same method. The black dot-dash line shows the ordinary linear regression between gas velocity dispersion and redshift for the combined data. The grey dashed line is a robust $\sigma_{\text{gas}} - z$ linear relation (Cappellari et al. 2013) from Figure. 6 in Übler et al. (2019), fitted using the ionised gas velocity dispersion data from literature at $0 < z < 4$. This plot shows that the gas velocity dispersions of SAMI, MAGPI and KROSS galaxies are consistent with the decreasing trend of gas velocity dispersion over cosmic time suggested by previous studies (Kassin et al. 2012; Wisnioski et al. 2015; Übler et al. 2019).

the gas-rich galaxies have a relatively shortlived feature of 3-arm ($m = 3$) spirals using hydrodynamics simulations. They suggested that this feature is indicative of large-scale instability in the disc’s early lifecycle. Two galaxies (ID=1202197197, 1204198199) with $m = 3$ pattern are identified as three-armed spiral galaxies in Chen et al. (2023). Based on the white light MUSE image, another one (ID=1528197197) has some features of spiral arms, but the number of arms is uncertain. The remaining $m = 3$ galaxy (ID=1503208231) does not have a clear feature of arms. Finally, for these $m = 3$ featured galaxies, the possible influence of AGN-driven turbulence cannot be ruled out completely.

Mechanisms acting on different scales, such as stellar feedback, gas transportation and accretion, may contribute to the gas turbulence at the same time. However, simulating physical processes at different scales at the same time is difficult and simulations on different scales give different results. Using magnetohydrodynamic simulations of the star-forming interstellar medium in galaxy discs, Rathjen et al. (2023) showed the correlation between gas velocity dispersion and SFR vanished if they turned off stellar feedback. In contrast, Jiménez et al. (2023) showed that the correlation is weaker but still exists in their EAGLE cosmological simulations without star-formation feedback. Note that these two studies investigate the relation in different

scales. Rathjen et al. (2023) focused on a galactic scale and did not include the impact of cosmological accretion on turbulence. On the contrary, Jiménez et al. (2023) studied the impact of several mechanisms on turbulence on cosmological scales, but their results were limited by the spatial resolution of cosmological simulations and the sub-grid physics that was employed for stellar feedback.

The importance of different mechanisms may also vary with redshift and halo mass (Ginzburg et al. 2022; Jiménez et al. 2023). Ginzburg et al. (2022) built an analytical model to show that the contributions from three mechanisms to gas turbulence, including stellar feedback, gas transportation and gas accretion, evolved with cosmic time and were different for galaxies in different halo masses, but the relative contributions between them (the ratio of turbulent energy injection rates between different processes) were within a factor of ~ 2 in all discs at all redshifts. Their model predicts that stellar feedback is relatively more important for galaxies in lower halo mass and at lower redshift. The importance of gas transportation increases with redshift. Accretion is the most important mechanism for galaxies at $z > 3$. Similarly, Kohandel et al. (2020) used zoom-in simulations of galaxies to show accretion and mergers are the major sources of gas velocity dispersion for galaxies at $6 < z < 8$ and stellar feedback is sub-dominant.

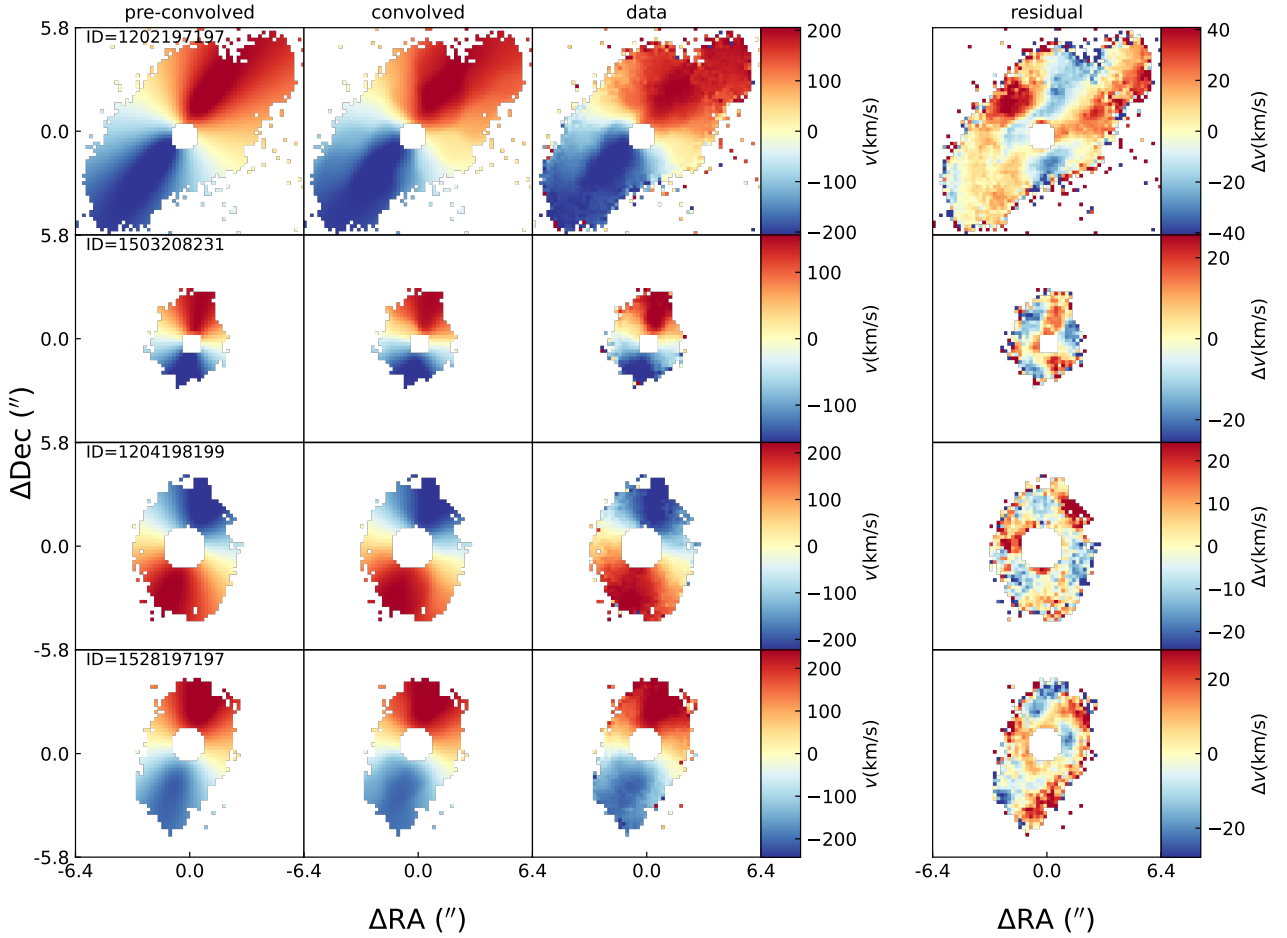


Figure 10. Four MAGPI galaxies that have $m = 3$ Fourier mode in the velocity residual maps. The first column shows the model made by `BLOBBY3D`; the second column shows the model convolved with the PSF and LSF of the data; the third column shows the results of the single Gaussian fit to the observed datacube; the fourth column shows the residuals between the data and the convolved model.

Our results support a multi-drivers scenario. Both MAGPI and SAMI galaxies have a strong correlation between gas velocity dispersion and Σ_{SFR} , agreeing with [Ginzburg et al. \(2022\)](#)'s model that the gas velocity dispersion is predominantly supported by stellar feedback at low redshift. They also showed that the importance of transportation and accretion slowly increases with redshift, which is consistent with our result in Figure 6 that the gas velocity dispersion is correlated with the non-rotational motion of gas (Δv) for MAGPI galaxies and the correlation coefficient between Δv and σ_{gas} ($r = 0.424$) is smaller than that of Σ_{SFR} and σ_{gas} ($r = 0.71$). [Ginzburg et al. \(2022\)](#) also showed that for galaxies at $z \sim 1$, the contribution of gas transportation is similar to stellar feedback. Stellar feedback is relatively more important for galaxies in haloes with a halo mass $\log M_{h,0} \lesssim 12.5$ at $z = 0$, while gas transportation is more important for galaxies in haloes with $\log M_{h,0} \gtrsim 12.5$. KROSS galaxies have ~ 1 dex higher stellar mass on average than MAGPI and SAMI galaxies, which implies that they tend to live in higher mass haloes. This fact may be why we see a weaker correlation ($r = 0.29$) between gas velocity dispersion and Σ_{SFR} for the KROSS galaxies and the scatter of gas velocity dispersion in the Σ_{SFR} bin is higher than SAMI and MAGPI. However, we note that the range of Σ_{SFR} of KROSS galaxies on a log-scale is ~ 1 dex narrower than SAMI and MAGPI, which may limit our ability to detect the correlation. It is worth exploring the gas velocity dispersion of low mass high redshift galaxies.

6 CONCLUSIONS

We studied the intrinsic $\text{H}\alpha$ kinematic properties of 110 galaxies at $z \sim 0.3$ from the MAGPI survey using a 3D Bayesian inference forward-modelling technique, `BLOBBY3D`, which can model gas kinematics and gas substructure simultaneously. It assumes a regular rotating disc and decomposes the ionised gas distribution into a number of blobs with a positive definite Gaussian basis function. The constructed 3D cubes are convolved by the PSF and LSF to account for the beam smearing and instrumental broadening. The average gas velocity dispersion at $z \sim 0.3$ is found to be $26.1 \pm 8.7 \text{ km s}^{-1}$, where $\pm 8.7 \text{ km s}^{-1}$ represents the standard deviation.

We investigate the correlation between the gas velocity dispersion of MAGPI galaxies and galaxy properties. We find the gas velocity dispersion of MAGPI galaxies has the strongest correlation with Σ_{SFR} ($r = 0.65$). The gas velocity dispersion also has a strong correlation with SFR ($r = 0.46$) and with ΔSFR ($r = 0.50$). The partial correlation analysis between gas velocity dispersion, SFR, stellar mass and galaxy size shows that dispersion has a positive partial correlation with SFR and a negative partial correlation with size and an insignificant correlation with stellar mass. Using the residual between the regular rotating velocity map in the model and the velocity map of galaxies as an indicator of the non-rotational motion of the

gas, we find the galaxies with higher velocity residual tend to have higher gas velocity dispersion.

We compare our results of MAGPI galaxies ($z \sim 0.3$) with SAMI ($z \sim 0.05$) and KROSS ($z \sim 1$) survey, for which the gas velocity dispersion is also measured using `BLOBBY3D`. The σ_{gas} -lookback time relation shows a decreasing trend of gas velocity dispersion over cosmic time. Both SAMI and MAGPI galaxies have a strong correlation between σ_{gas} and Σ_{SFR} . KROSS galaxies have a moderate correlation between σ_{gas} and Σ_{SFR} . We find that σ_{gas} is similar at fixed Σ_{SFR} for SAMI, MAGPI and KROSS galaxies, which suggests that the mechanisms related to Σ_{SFR} may be the dominant factor that drives gas turbulence from $z \sim 1$ to $z \sim 0$. The possible mechanisms that can explain this σ_{gas} - Σ_{SFR} correlation are stellar feedback and gravitational instability.

When compared with theoretical models, our results support a multi-drivers scenario. At $z \sim 0.05$ and $z \sim 0.3$, the star-formation feedback is the dominant driver of gas turbulence. The correlation between Δv and σ_{gas} suggests that the non-rotational motion of the gas, such as gas transportation through the disc or gas accretion, also contributes to the gas turbulence for MAGPI galaxies at $z \sim 0.3$. For KROSS galaxies at $z \sim 1$, the importance of gas transportation may be higher than at low redshift, resulting in the moderate correlation between dispersion and Σ_{SFR} and higher scatter of σ_{gas} in the Σ_{SFR} bin.

ACKNOWLEDGEMENTS

We wish to thank the ESO staff, and in particular the staff at Paranal Observatory, for carrying out the MAGPI observations. MAGPI targets were selected from GAMA. GAMA is a joint European-Australasian project based around a spectroscopic campaign using the Anglo-Australian Telescope. GAMA was funded by the STFC (UK), the ARC (Australia), the AAO, and the participating institutions. GAMA photometry is based on observations made with ESO Telescopes at the La Silla Paranal Observatory under programme ID 179.A-2004, ID 177.A-3016. The MAGPI team acknowledge support by the Australian Research Council Centre of Excellence for All Sky Astrophysics in 3 Dimensions (ASTRO 3D), through project number CE170100013. YM is supported by an Australian Government Research Training Program (RTP) Scholarship. CF is the recipient of an Australian Research Council Future Fellowship (project number FT210100168) funded by the Australian Government. CL, JTM and CF are the recipients of ARC Discovery Project DP210101945. KG is supported by the Australian Research Council through the Discovery Early Career Researcher Award (DECRA) Fellowship (project number DE220100766) funded by the Australian Government. Y.P. acknowledges the support from the National Science Foundation of China (NSFC) grant Nos. 12125301, 12192220, 12192222, and the science research grants from the China Manned Space Project with No. CMS-CSST-2021-A07. GS and KH acknowledge funding from the Australian Research Council (ARC) Discovery Project DP210101945. SMS acknowledges funding from the Australian Research Council (DE220100003). LMV acknowledges support by the German Academic Scholarship Foundation (Studienstiftung des deutschen Volkes) and the Marianne-Plehn-Program of the Elite Network of Bavaria. M.V. was supported by philanthropic funding from The Johnston Fellowship and from other donor(s) who are families affected by mental illness who wish to remain anonymous.

DATA AVAILABILITY

The MUSE data used in this work are available on the ESO public archive. The reduced MAGPI datacubes and the emission line data products will be public in the MAGPI team data release (Mendel et al. in prep and Battisti et al. in prep).

REFERENCES

- Aumer M., Burkert A., Johansson P. H., Genzel R., 2010, *ApJ*, **719**, 1230
 Bacchini C., Fraternali F., Iorio G., Pezzulli G., Marasco A., Nipoti C., 2020, *A&A*, **641**, A70
 Bacon R., et al., 2010, in McLean I. S., Ramsay S. K., Takami H., eds, Society of Photo-Optical Instrumentation Engineers (SPIE) Conference Series Vol. 7735, Ground-based and Airborne Instrumentation for Astronomy III, p. 773508, doi:10.1117/12.856027
 Bacon R., et al., 2017, *A&A*, **608**, A1
 Baldwin J. A., Phillips M. M., Terlevich R., 1981, *PASP*, **93**, 5
 Bekiaris G., Glazebrook K., Fluke C. J., Abraham R., 2016, *MNRAS*, **455**, 754
 Bellstedt S., et al., 2020, *MNRAS*, **498**, 5581
 Bertin G., Lodato G., 1999, *A&A*, **350**, 694
 Bik A., Östlin G., Hayes M., Melinder J., Menacho V., 2022, *A&A*, **666**, A161
 Bird J. C., Loebman S. R., Weinberg D. H., Brooks A. M., Quinn T. R., Christensen C. R., 2021, *MNRAS*, **503**, 1815
 Bittner A., et al., 2019, *A&A*, **628**, A117
 Bland-Hawthorn J., Tepper-García T., 2021, *MNRAS*, **504**, 3168
 Bland-Hawthorn J., et al., 2011, *Optics Express*, **19**, 2649
 Bland-Hawthorn J., Tepper-García T., Agertz O., Federrath C., 2024, *ApJ*, **968**, 86
 Bouché N., et al., 2010, *ApJ*, **718**, 1001
 Bouché N., Carfanton H., Schroetter I., Michel-Dansac L., Contini T., 2015, *AJ*, **150**, 92
 Bournaud F., Elmegreen B. G., Martig M., 2009, *ApJ*, **707**, L1
 Bower R. G., Benson A. J., Malbon R., Helly J. C., Frenk C. S., Baugh C. M., Cole S., Lacey C. G., 2006, *MNRAS*, **370**, 645
 Brewer B. J., Foreman-Mackey D., 2018, *Journal of Statistical Software*, **86**, 1–33
 Brewer B. J., Pártay L. B., Csányi G., 2011, *Statistics and Computing*, **21**, 649
 Bruzual G., Charlot S., 2003, *MNRAS*, **344**, 1000
 Bryant J. J., et al., 2015, *MNRAS*, **447**, 2857
 Cappellari M., 2016, *ARA&A*, **54**, 597
 Cappellari M., 2017, *MNRAS*, **466**, 798
 Cappellari M., Emsellem E., 2004, *PASP*, **116**, 138
 Cappellari M., et al., 2013, *MNRAS*, **432**, 1709
 Cardelli J. A., Clayton G. C., Mathis J. S., 1989, *ApJ*, **345**, 245
 Ceverino D., Primack J., Dekel A., Kassin S. A., 2017, *MNRAS*, **467**, 2664
 Chabrier G., 2003, *PASP*, **115**, 763
 Charlot S., Fall S. M., 2000, *ApJ*, **539**, 718
 Chen Q.-H., et al., 2023, *arXiv e-prints*, p. arXiv:2310.20073
 Conroy C., Gunn J. E., 2010, *ApJ*, **712**, 833
 Conroy C., Gunn J. E., White M., 2009, *ApJ*, **699**, 486
 Conroy C., White M., Gunn J. E., 2010, *ApJ*, **708**, 58
 Cortese L., et al., 2016, *MNRAS*, **463**, 170
 Courteau S., 1997, *AJ*, **114**, 2402
 Croom S. M., et al., 2012, *MNRAS*, **421**, 872
 Croom S. M., et al., 2021, *MNRAS*, **505**, 991
 Davé R., Finlator K., Oppenheimer B. D., 2012, *MNRAS*, **421**, 98
 Davies R., et al., 2011, *ApJ*, **741**, 69
 Dekel A., Sari R., Ceverino D., 2009, *ApJ*, **703**, 785
 Di Teodoro E. M., Fraternali F., 2015, *MNRAS*, **451**, 3021
 Dib S., Bell E., Burkert A., 2006, *ApJ*, **638**, 797
 Driver S. P., et al., 2011, *MNRAS*, **413**, 971
 Egorov O. V., et al., 2023, *arXiv e-prints*, p. arXiv:2307.10277
 Epinat B., Amram P., Marcelin M., 2008, *MNRAS*, **390**, 466

- Epinat B., Amram P., Balkowski C., Marcelin M., 2010, *MNRAS*, **401**, 2113
- Faucher-Giguère C.-A., Quataert E., Hopkins P. F., 2013, *MNRAS*, **433**, 1970
- Fitzpatrick E. L., Massa D., Gordon K. D., Bohlin R., Clayton G. C., 2019, *ApJ*, **886**, 108
- Forbes J., Krumholz M., Burkert A., 2012, *ApJ*, **754**, 48
- Forbes J. C., Krumholz M. R., Burkert A., Dekel A., 2014, *MNRAS*, **438**, 1552
- Forbes J. C., et al., 2023, *ApJ*, **948**, 107
- Foster C., et al., 2021, *Publ. Astron. Soc. Australia*, **38**, e031
- Fusco T., et al., 2020, *A&A*, **635**, A208
- Gabor J. M., Bournaud F., 2014, *MNRAS*, **437**, L56
- Genel S., Dekel A., Cacciato M., 2012, *MNRAS*, **425**, 788
- Genzel R., et al., 2006, *Nature*, **442**, 786
- Genzel R., et al., 2017, *Nature*, **543**, 397
- Genzel R., et al., 2023, *ApJ*, **957**, 48
- Ginzburg O., Dekel A., Mandelker N., Krumholz M. R., 2022, *MNRAS*, **513**, 6177
- Grand R. J. J., et al., 2016, *MNRAS*, **460**, L94
- Green A. W., et al., 2010, *Nature*, **467**, 684
- Green A. W., et al., 2014, *MNRAS*, **437**, 1070
- Harrison C. M., et al., 2017, *MNRAS*, **467**, 1965
- Hopkins A. M., Beacom J. F., 2006, *ApJ*, **651**, 142
- Hung C.-L., et al., 2019, *MNRAS*, **482**, 5125
- Jiménez E., Lagos C. d. P., Ludlow A. D., Wisnioski E., 2023, *MNRAS*, **524**, 4346
- Johnson H. L., et al., 2018, *MNRAS*, **474**, 5076
- Kassin S. A., et al., 2012, *ApJ*, **758**, 106
- Kauffmann G., et al., 2003, *MNRAS*, **346**, 1055
- Kawata D., Hunt J. A. S., Grand R. J. J., Pasetto S., Cropper M., 2014, *MNRAS*, **443**, 2757
- Kennicutt Robert C. J., 1998, *ARA&A*, **36**, 189
- Kennicutt R. C., Evans N. J., 2012, *ARA&A*, **50**, 531
- Kewley L. J., Dopita M. A., Sutherland R. S., Heisler C. A., Trevena J., 2001, *ApJ*, **556**, 121
- Khachatryan T., Beraldo e Silva L., Debattista V. P., Daniel K. J., 2022, *MNRAS*, **512**, 3500
- Kim C.-G., Ostriker E. C., Kim W.-T., 2013, *ApJ*, **776**, 1
- Klessen R. S., Hennebelle P., 2010, *A&A*, **520**, A17
- Kohandel M., Pallottini A., Ferrara A., Carniani S., Gallerani S., Vallini L., Zanella A., Behrens C., 2020, *MNRAS*, **499**, 1250
- Krumholz M., Burkert A., 2010, *ApJ*, **724**, 895
- Krumholz M. R., Burkert B., 2016, *MNRAS*, **458**, 1671
- Krumholz M. R., Kruijssen J. M. D., Crocker R. M., 2017, *MNRAS*, **466**, 1213
- Krumholz M. R., Burkert B., Forbes J. C., Crocker R. M., 2018, *MNRAS*, **477**, 2716
- Law D. R., Steidel C. C., Erb D. K., Larkin J. E., Pettini M., Shapley A. E., Wright S. A., 2009, *ApJ*, **697**, 2057
- Law D. R., et al., 2022, *ApJ*, **928**, 58
- Lehnert M. D., Le Tiran L., Nesvadba N. P. H., van Driel W., Boulanger F., Di Matteo P., 2013, *A&A*, **555**, A72
- Leslie S. K., et al., 2020, *ApJ*, **899**, 58
- Lilly S. J., Carollo C. M., Pipino A., Renzini A., Peng Y., 2013, *ApJ*, **772**, 119
- Madau P., Dickinson M., 2014, *ARA&A*, **52**, 415
- Madau P., Pozzetti L., Dickinson M., 1998, *ApJ*, **498**, 106
- Moiseev A. V., Tikhonov A. V., Klypin A., 2015a, *MNRAS*, **449**, 3568
- Moiseev A. V., Tikhonov A. V., Klypin A., 2015b, *MNRAS*, **449**, 3568
- Molina J., et al., 2020, *A&A*, **643**, A78
- Mun M., et al., 2024, *MNRAS*,
- Oh S., et al., 2022, *MNRAS*, **512**, 1765
- Oliva-Altamirano P., Fisher D. B., Glazebrook K., Wisnioski E., Bekiaris G., Bassett R., Obreschkow D., Abraham R., 2018, *MNRAS*, **474**, 522
- Ostriker E. C., Shetty R., 2011, *ApJ*, **731**, 41
- Ostriker E. C., McKee C. F., Leroy A. K., 2010, *ApJ*, **721**, 975
- Peng C. Y., Ho L. C., Impey C. D., Rix H.-W., 2010, *AJ*, **139**, 2097
- Popesso P., et al., 2023, *MNRAS*, **519**, 1526
- Rathjen T.-E., Naab T., Walch S., Seifried D., Girichidis P., Wunsch R., 2023, *MNRAS*, **522**, 1843
- Robotham A. S. G., Davies L. J. M., Driver S. P., Koushan S., Taranu D. S., Casura S., Liske J., 2018, *MNRAS*, **476**, 3137
- Robotham A. S. G., Bellstedt S., Lagos C. d. P., Thorne J. E., Davies L. J., Driver S. P., Bravo M., 2020, *MNRAS*, **495**, 905
- Schaye J., et al., 2015, *MNRAS*, **446**, 521
- Scott N., et al., 2018, *MNRAS*, **481**, 2299
- Sharples R., et al., 2013, *The Messenger*, **151**, 21
- Shetty R., Ostriker E. C., 2012, *ApJ*, **754**, 2
- Sillero E., Tissera P. B., Lambas D. G., Michel-Dansac L., 2017, *MNRAS*, **472**, 4404
- Skilling J., 2004, in Fischer R., Preuss R., Toussaint U. V., eds, *American Institute of Physics Conference Series Vol. 735, Bayesian Inference and Maximum Entropy Methods in Science and Engineering: 24th International Workshop on Bayesian Inference and Maximum Entropy Methods in Science and Engineering*. pp 395–405, doi:10.1063/1.1835238
- Stott J. P., et al., 2016, *MNRAS*, **457**, 1888
- Sun J., et al., 2020, *ApJ*, **892**, 148
- Tacconi L. J., Genzel R., Sternberg A., 2020, *ARA&A*, **58**, 157
- Taylor E. N., et al., 2011, *MNRAS*, **418**, 1587
- Tepper-García T., Bland-Hawthorn J., Freeman K., 2022, *MNRAS*, **515**, 5951
- Toomre A., 1964, *ApJ*, **139**, 1217
- Tsukui T., Wisnioski E., Bland-Hawthorn J., Mai Y., Iguchi S., Baba J., Freeman K., 2024, *MNRAS*, **527**, 8941
- Übler H., et al., 2019, *ApJ*, **880**, 48
- Vallat R., 2018, *Journal of Open Source Software*, **3**, 1026
- Varidel M. R., et al., 2019, *MNRAS*, **485**, 4024
- Varidel M. R., et al., 2020, *MNRAS*, **495**, 2265
- Weijmans A.-M., et al., 2014, *MNRAS*, **444**, 3340
- Wiklund T., et al., 2019, *ApJ*, **878**, 83
- Wisnioski E., et al., 2015, *ApJ*, **799**, 209
- Wuyts S., et al., 2011, *ApJ*, **738**, 106
- Yu X., et al., 2019, *MNRAS*, **486**, 4463
- Zhou L., et al., 2017, *MNRAS*, **470**, 4573
- da Cunha E., Charlot S., Elbaz D., 2008, *MNRAS*, **388**, 1595

This paper has been typeset from a $\text{\TeX}/\text{\LaTeX}$ file prepared by the author.